JOURNAL OF THE ROYAL SOCIETY Interface

FirstCite® e-publishing

J. R. Soc. Interface
doi:10.1098/rsif.2010.0678
Published online

Mechanical models of sandfish locomotion reveal principles of high performance subsurface sand-swimming

Ryan D. Maladen[1], Yang Ding[2], Paul B. Umbanhowar[3], Adam Kamor[2] and Daniel I. Goldman[1,2,*]

[1]*Bioengineering Program, and* [2]*School of Physics, Georgia Institute of Technology, Atlanta, GA 30332–0250, USA*
[3]*Department of Mechanical Engineering, Northwestern University, Evanston, IL 60208, USA*

We integrate biological experiment, empirical theory, numerical simulation and a physical model to reveal principles of undulatory locomotion in granular media. High-speed X-ray imaging of the sandfish lizard, *Scincus scincus*, in 3 mm glass particles shows that it swims within the medium without using its limbs by propagating a single-period travelling sinusoidal wave down its body, resulting in a wave efficiency, η, the ratio of its average forward speed to the wave speed, of approximately 0.5. A resistive force theory (RFT) that balances granular thrust and drag forces along the body predicts η close to the observed value. We test this prediction against two other more detailed modelling approaches: a numerical model of the sandfish coupled to a discrete particle simulation of the granular medium, and an undulatory robot that swims within granular media. Using these models and analytical solutions of the RFT, we vary the ratio of undulation amplitude to wavelength (A/λ) and demonstrate an optimal condition for sand-swimming, which for a given A results from the competition between η and λ. The RFT, in agreement with the simulated and physical models, predicts that for a single-period sinusoidal wave, maximal speed occurs for $A/\lambda \approx 0.2$, the same kinematics used by the sandfish.

Keywords: locomotion; granular; modelling; robot; lizard; swimming

1. INTRODUCTION

Discovering principles of locomotion for organisms in natural environments requires integrating experimental visualization [1–4], theoretical [5–7], computational [8–10] and robotic [11–14] approaches to generate and test hypotheses of interaction between a locomotor and its surroundings [9,15–17]. These approaches have produced an understanding of locomotion biomechanics in a range of terrestrial, aquatic and aerial environments [18–21]. Comparable analysis of locomotion within yielding substrates like sand, soil and debris that display both solid and fluid-like behaviour is less developed [9,22–25]. This is, in part, because visualizing motion in opaque materials is challenging, and validated force models on and within these substrates at the level of those that exist for fluids (see [19,26,27]) do not exist yet.

Attempts to understand burrowing and movement within granular media like desert sand directly confront these issues. Subsurface locomotor behaviours are relevant to a diversity of organisms, such as scorpions, snakes and lizards, that move within the sand to escape heat and predators, and to hunt [28–30]. To answer questions about ecological adaptations [28,31–33] and evolution [34–36] in flowing substrates requires an understanding of how propulsion is generated and how both media interactions and animal kinematics enhance or limit locomotor performance.

Recently, we used high-speed X-ray imaging to visualize the locomotion of a small desert lizard, the sandfish, *Scincus scincus*, within approximately spherical 0.3 mm diameter glass particles, a granular medium representative of desert sands [37]. We found that once it buries rapidly (within one-half of a second) into the sand, the animal swims subsurface at up to $2\,\mathrm{bl\,s^{-1}}$ (bl, body-length is defined as the distance from the snout tip to the base of the tail) by propagating a sinusoidal wave down its body (anterior to posterior) without using its limbs [22]. The animal monotonically increases speed by increasing its oscillation frequency while using the same undulatory kinematics (a single-period sinusoidal travelling wave with an amplitude to wavelength ratio of approximately 0.2) even within media prepared to different initial yield strengths (controlled via volume fraction or 'media compaction').

Developing models to describe subsurface locomotion requires understanding resistive forces on

*Author for correspondence (daniel.goldman@physics.gatech.edu).

Electronic supplementary material is available at http://dx.doi.org/10.1098/rsif.2010.0678 or via http://rsif.royalsocietypublishing.org.

Received 30 November 2010
Accepted 28 January 2011

intruders and how intruders change the local properties of the media [38]. As a broadly applicable theory of intrusion into granular media does not yet exist in the regime relevant to sand-swimming, in the study of Maladen *et al.* [22] an empirical resistive force theory (RFT) was developed to predict the wave efficiency η—the ratio of the forward swimming speed to the wave speed. The granular RFT was inspired by the theory used to predict swimming speeds of micro-organisms [39] in fluids at low Reynolds numbers (Re), where inertial effects are small, and balances empirically measured estimates of drag and thrust forces on elements of the animal. The RFT demonstrated that body undulations are sufficient to propel the sandfish forward, and its prediction of η was close to the observed η.

The RFT predictions are based on a simplified model of the animal kinematics and an empirical model of the granular resistive forces on the body. In this paper, we describe the development of two, more detailed and flexible models of undulatory sand-swimming that reproduce the observed biological sand-swimming and exhibit performance in accord with predictions of the RFT. In the first, a computer simulation approach, we couple a numerical model of the sandfish with a multi-particle discrete element method (DEM) [40] simulation of the granular medium. In the second approach, we measure the locomotor performance of a physical model (a robot). We use all three models to study how the wave kinematics of the rapidly escaping sandfish maximize forward swimming speed within the granular media. More generally, these complementary modelling approaches will allow us to explore and answer questions about undulatory locomotion in complex, yielding media.

2 BIOLOGICAL EXPERIMENTS

We use an air-fluidized bed to control the initial preparation of the material. The packing state of the substrate is parametrized by the volume fraction ϕ, the ratio of solid to occupied volume [41] of the granular medium. The fluidized bed is a box of area 21.5 cm × 18 cm with a porous base and is filled with granular material 10 cm deep. A continuous flow of air through the base expands the granular medium in the bed to a low ϕ state; subsequent pulses of air increase compaction allowing precise control of the initial volume fraction of the bed. All air flow through the bed is turned off before the animal is released onto the medium. We use high-speed X-ray imaging to record the movement of the sandfish, *Scincus scincus*, as it swims subsurface (for further experimental details, see [22]).

In the work of Maladen *et al.* [22], we studied sandfish locomotion within 0.27 ± 0.04 mm diameter approximately spherical glass particles, close in size to the sand found in the animal's natural environment [42]. Here, we study swimming in larger spherical glass particles (diameter: 3.2 ± 0.2 mm, referred to here as '3 mm particles') to reduce the time required to simulate the granular medium (figure 1*a*,*b*). High-speed X-ray imaging experiments reveal that the sandfish (five animals; mass = 16.9 ± 4.0 g; body-length (bl) $L = 8.8 \pm 3.3$ cm) swims subsurface in the 3 mm particles with performance comparable to that in the 0.3 mm particles. The sandfish are tested in loosely ($\phi = 0.60$) and closely ($\phi = 0.62$) packed media preparations and take 1.2 ± 0.6 s to complete the burial process (time from entry until tail is not visible) independent of media preparation. Interestingly, although swimming performance is comparable in the two bead sizes, the burial time in the 3 mm particles is significantly longer than in the 0.3 mm particles. Once subsurface, the animal places its limbs along its sides and advances by executing an undulatory motion (see electronic supplementary material, movie S1). We quantify the subsurface motion by tracking the mid-line of the animal.

As in the study of Maladen *et al.* [22], all phases of the undulatory motion of the animal midline are well-fit by a posteriorly travelling single-period sinusoidal wave ($R^2 > 0.9$)

$$y = A \sin \frac{2\pi}{\lambda}(x + v_w t), \tag{2.1}$$

with y the displacement from the mid-line of a straight animal, A the amplitude, λ the wavelength, f the wave frequency, $v_w = f\,\lambda$ the wave speed, t the time and x the distance along a line joining the endpoints of the animal and parallel to the direction of motion. The x and y coordinates are set in the laboratory frame. The number of periods along the body of the swimming animal, ξ, is approximately 1.0 in experiment. The spatial characteristics of the wave, A and λ, do not vary significantly within a run or between runs and their ratio is conserved at approximately $A/\lambda = 0.25 \pm 0.07$. A (average 0.18 ± 0.03 bl, $p = 0.26$) and λ (average 0.7 ± 0.1 bl, $p = 0.13$) are not significantly different for loosely and closely packed media preparations. A p-value greater than 0.05 indicates that no statistically different relation exists between the measured values for the different conditions tested [43]. As within 0.3 mm particles [22], the animal increases its forward velocity by increasing its undulation frequency (figure 1*d*).

A measure of performance of undulatory locomotion in deformable media is the wave efficiency (also referred to as the 'amount of slip'; [44]), η, the ratio between the average forward velocity of the animal v_x and the velocity of the wave travelling down its body v_w. Typical values of η for small organisms (such as nematodes) for whom inertial effects are negligible are 0.22 ± 0.02, while swimming in fluids at low Re [39] and 0.8–0.9 while creeping along an air–solid interface [44–46]. Because A/λ for sandfish is independent of f, η is the slope of the v_x/λ versus f curve (figure 1*d*). For 3 mm particles, $\eta = 0.54 \pm 0.13$ (figure 1*d*,*e*), similar to the value of 0.52 ± 0.02 for locomotion in 0.3 mm particles [22]. For both particle sizes, η is independent of media preparation.

3. RESISTIVE FORCE THEORY FOR GRANULAR MEDIA

We use a previously developed RFT [22] for granular media to predict η. The RFT assumes that the animal swims in a horizontal plane, although it actually moves into the medium at an angle relative to the horizontal of approximately 22° in 0.3 mm particles [22] and approximately 29° in the 3 mm particles. We discuss the validity of this assumption in §7. In RFT models, the body of the locomotor is partitioned into infinitesimal elements along its

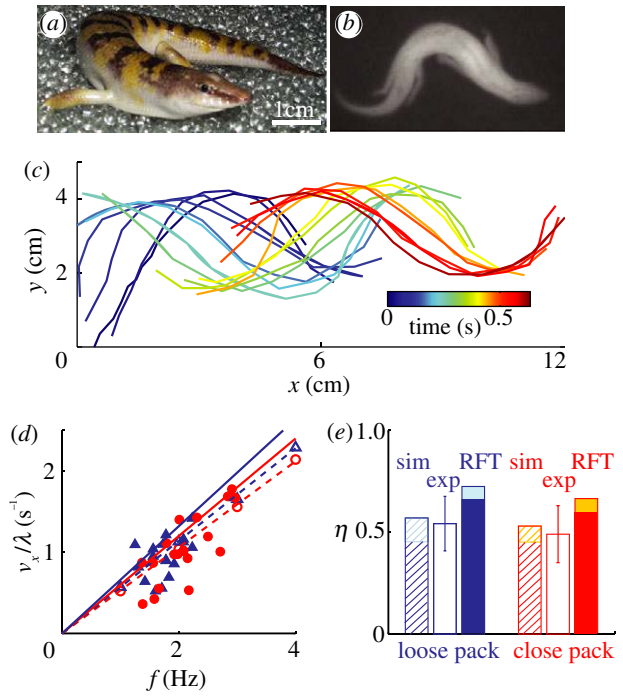

Figure 1. Kinematics, speed and wave efficiency of the sand-swimming sandfish lizard *Scincus scincus* and predictions from granular resistive force theory (RFT) and numerical simulation. (*a*) The sandfish lizard on 3 mm glass particles. (*b*) X-ray image of sandfish swimming subsurface in 0.3 mm glass particles. (*c*) Tracked mid-line of the sandfish shows the kinematics as it propels itself using body undulations within a granular medium of 3 mm glass particles. (*d*) Average forward swimming speed versus undulation frequency in 3 mm particles. Solid symbols refer to biological measurements, and the solid and dashed lines correspond to the RFT (for a flat head) and simulation (for a tapered head) predictions, respectively. (*e*) Wave efficiency (η), the ratio of the forward swimming speed to the wave speed as determined from the slope of v_x/λ versus f measured in (*d*) for biological data, RFT and numerical simulation in 3 mm particles. For the RFT (solid colours), the lower and upper limits of the η deviation (cyan (loosely packed) and (orange (closely packed)) correspond to maximum (flat head) and 30 per cent of the maximum head drag, while the simulation (hatched) corresponds to the flat and tapered head shapes, respectively. Blue and red colours in (*d*) and (*e*) correspond to loosely and closely packed media preparations, respectively.

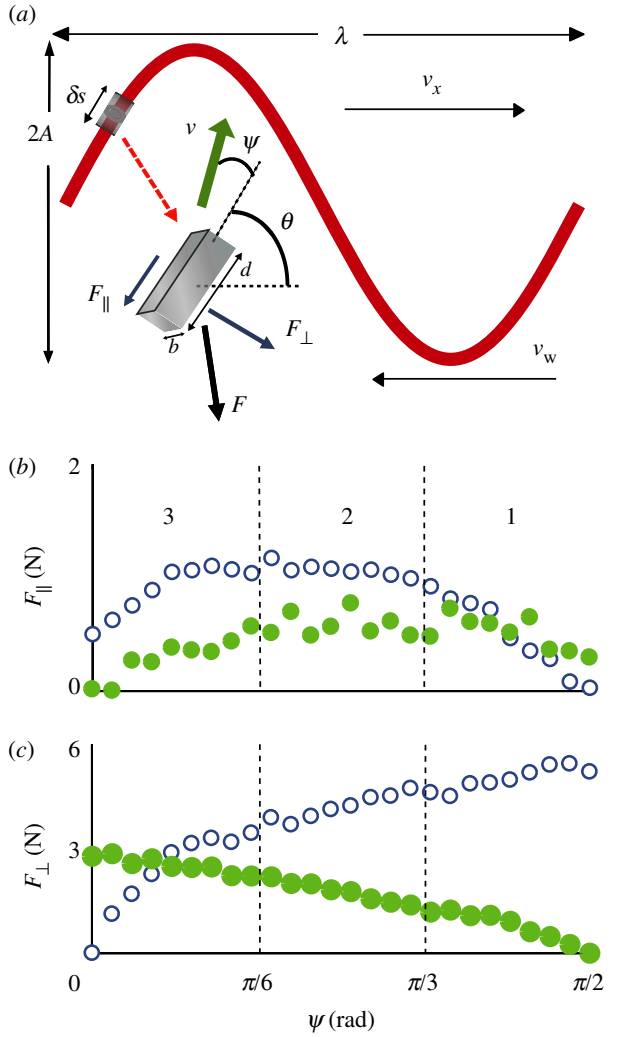

Figure 2. Resistive force theory (RFT) for granular media in which the sandfish is (*a*) approximated by a square cross-section tube along which a single period sinusoidal travelling wave propagates head to tail. As the tube moves through the medium, a force acts on each element of the tube and the force is resolved into parallel ($F_\parallel$) and perpendicular ($F_\perp$) components. δs and d refer to the length of the element in the RFT and drag experiments, respectively. (*b*) $F_\parallel$ and (*c*) $F_\perp$ from simulation of 3 mm glass particles on the length (blue open circles) and at the end caps (green closed circles) of the square cross-section rod as a function of the angle (ψ) between the velocity direction and the rod axis. Regions 1–3 separated by dashed black vertical lines correspond to similarly marked regions of the relationship between η and A/λ in figure 6*a*. (Online version in colour.)

length. When moving relative to the medium, each element is acted on by resistive forces (figure 2*a*) that can be decomposed into thrust and drag components. Resolving these forces into perpendicular ($F_\perp$) and parallel ($F_\parallel$) components, the net forward force on an element is

$$\delta F_x = \delta F_\perp \sin\theta - \delta F_\parallel \cos\theta, \tag{3.1}$$

where θ is the angle between the direction of the average velocity of the organism and the instantaneous orientation of the infinitesimal element. θ increases with the oscillation amplitude and can be obtained by differentiating equation (2.1):

$$\tan\theta = \frac{dy}{dx} = \frac{2A\pi}{\lambda}\cos\frac{2\pi}{\lambda}(x + v_w t). \tag{3.2}$$

For granular media, the force on an element is well characterized as a function of only the direction of the velocity relative to its orientation (ψ) since in the speed regime relevant to the animal previous studies, Maladen *et al.* [22], Albert *et al.* [47] and Wieghardt [48], showed that granular force is independent of speed. Determining the y-component of the velocity from equation (2.1)

$$v_y = \frac{dy}{dt} = \frac{2A\pi v_w}{\lambda}\cos\frac{2\pi}{\lambda}(x + v_w t) \tag{3.3}$$

allows us to write the angle ψ as

$$\psi = \tan^{-1}\left(\frac{v_y}{v_x}\right) - \theta. \tag{3.4}$$

The net forward force on the entire body is calculated by integrating the force on each element over the length of the body (snout to tail tip). Since the body propagates a single period wave ($\xi = 1$) and the force on a segment is assumed to be localized, propagation of the wave in essence moves a segment from one end of the body to the other end with the orientation, velocity and force on that segment unchanged. Therefore, the net force, the sum of the forces on all segments, is time-invariant. The drag on the forward surface of the head (element end cap), F_{head}, is averaged over a cycle. To estimate the average forward speed, the forces on the body and head are summed and set to zero. Assuming that the forces on an infinitesimal body element are proportional to the area of the sagittal cross section ($b\delta s$, where b is the height of the element, and $\delta s = \sqrt{1+\tan^2\theta}\,dx$ is the arc length) and are functions of ψ, the total time-averaged force on the sandfish can be expressed as:

$$\bar{F}_x = \int_0^{\lambda} (P_{\perp}\sin\theta - P_{\parallel}\cos\theta)\sqrt{1+\tan^2\theta}\,b\,dx + \bar{F}_{\mathrm{head}}, \tag{3.5}$$

where $P_{\perp}$ and $P_{\parallel}$ are stresses perpendicular and parallel to the axis of each element. By assuming a constant average velocity (net forward force along the body equal to zero), the speed of the organism and thus η can be determined. Motion and force only in the forward direction are considered.

Unlike in fluids, in an arbitrary granular medium, no validated theory exists to calculate the resistive forces on an element as a function of its angle relative to its velocity direction (ψ). Previously, Maladen *et al.* [22] obtained these force laws empirically at different ψ in 0.3 mm glass particles—the same granular medium in which the animal was tested in [22]. To estimate thrust and drag on the body and head of the organism (figure 2*a*), empirical fitting functions were used to separate the forces on the rod into terms describing the surface along the length (side) and end-cap of the rod.

Here, to avoid the approximations introduced by using empirical laws to resolve side and end-cap forces, we use a validated simulation of the granular medium to directly measure the surface forces acting on the dragged rod. The granular medium is simulated using a three-dimensional soft sphere discrete element methods (DEM) code [40]. To compute particle–particle and particle–intruder interaction forces, we calculate the normal force [49], F_n, and the tangential Coulomb friction force, F_s (see figure 3*c*) at each contact using

$$\left.\begin{aligned} F_n &= k\delta^{3/2} - G_n v_n \delta^{1/2} \\ \text{and} \qquad F_s &= \mu F_n, \end{aligned}\right\} \tag{3.6}$$

where δ is the virtual overlap between contacting particles, $v_n = (\vec{V}_1 - \vec{V}_2)\cdot\hat{n}$ (see figure 3*c*) is the normal component of relative velocity with $\hat{n}$ the unit vector along the line connecting the particles centers, and k and G_n represent the hardness and viscoelastic constants, respectively. μ refers to the particle–particle (μ_{pp}) or body–particle (μ_{bp}) friction coefficients depending on which objects are in contact. For specific values, see electronic supplementary material, table S1. The simulated medium (a 50 : 50 bi-disperse mixture of 3.4 and 3.0 mm glass particles, with density 2.47 g cm^{-3}, which we will refer to as 3 mm particles) is validated by comparing the forces on a cylindrical stainless steel rod (diameter = 1.6 cm, length = 4 cm) dragged horizontally through it with those from experiment (see electronic supplementary material, figure S1). Particle–particle restitution and friction coefficients are experimentally measured, while the hardness is selected such that particle overlap (δ) is less than 0.4 per cent of particle radius. The container holds a granular volume $25 \times 24 \times 17$ cm^3 in extent. We obtain a match between the force measured as the rod is dragged through the granular media in experiment and simulation as a function of time (see electronic supplementary material, figure S1*a*). The mean deviation between experimentally measured average drag force and simulated average drag force as a function of angle is less than 5 per cent (see electronic supplementary material, figure S1*b*).

The simulation allows direct measurement of the forces on the side and end caps of the rod separately from which we obtain $F_{\perp}$ and $F_{\parallel}$ (figure 2*b*,*c*). To estimate the effect of head drag, only forces on the leading end cap are considered. We note that $F_{\perp}$ and $F_{\parallel}$ are measured on a square cross-section rod (width, height $b = 1.6$ cm, length $d = 4$ cm), as we approximate the cross section of the sandfish as a square. The fitting functions used to obtain continuous functions from the discrete measurements of $F_{\perp}$ and $F_{\parallel}$ are reported in the electronic supplementary material. $P_{\perp}$ and $P_{\parallel}$ are obtained using the relation $P_{\perp} = F_{\perp}/bd$ and $P_{\parallel} = F_{\parallel}/bd$. We measure the forces within both loosely and closely packed media (see electronic supplementary material, figure S3).

To determine η using the RFT, we assume that the animal swims at constant speed, which implies that the net force integrated over the body is zero (i.e. $\bar{F}_x = 0$ in equation (3.5)). Substituting $F_{\perp}$ and $F_{\parallel}$ from the simulation and using the spatial characteristics of the animal, $A/\lambda = 0.22$ (close to the average A/λ measured in 0.3 [22] and 3 mm particles) and $\xi = 1$, we numerically solve equation (3.5) using an unconstrained nonlinear optimization, which finds the minimum of a scalar function of several variables starting at an initial estimate. With a flat head (maximum drag) this procedure yields $\eta = 0.66$ in loosely packed and $\eta = 0.59$ in closely packed media; both values are larger than that measured for the animal ($\eta = 0.54 \pm 0.13$; figure 1*d*,*e*). We discuss this difference in §7.

4. NUMERICAL AND ROBOTIC MODELLING APPROACHES

To better model the animal and test the predictions of the RFT, we develop two complementary models of the sandfish in which parameters can be readily varied: a numerical simulation that combines a model of the animal with the validated granular medium model, and a sandfish inspired physical robot that is tested in a granular medium. These tools also allow us to investigate the effects of varying parameters like A, λ and ξ, variables which we have no control over in the biological experiment (§2). First we describe the development of the modelling approaches and compare their predictions of η to the

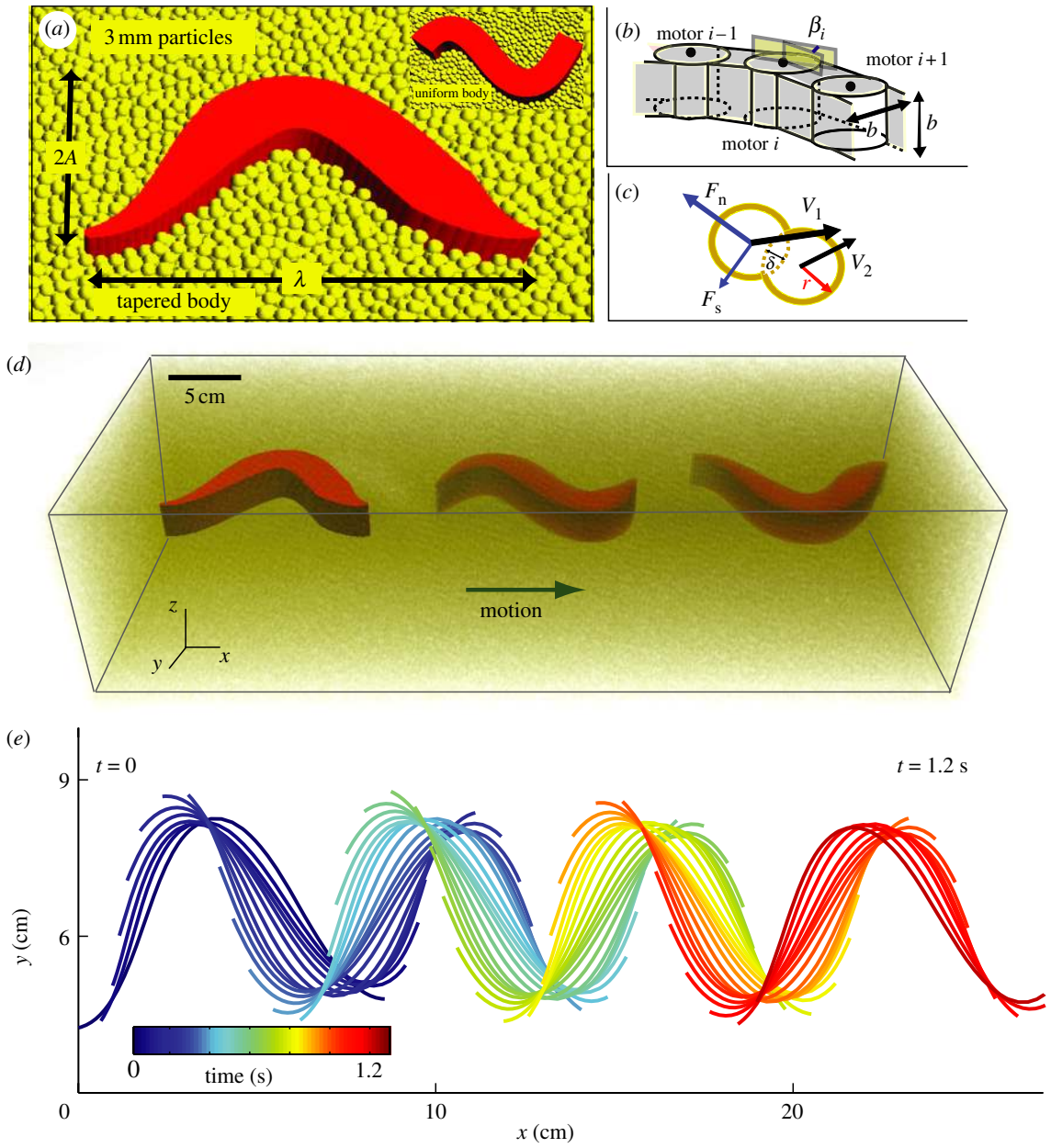

Figure 3. Numerically simulated model of the sandfish (figure 1*a*). (*a*) Close-up view of the numerical sandfish with tapered body cross section (approximating that of the animal) in 3 mm glass particles (particles above the sandfish model are rendered transparent). Inset shows the numerical sandfish with uniform body cross section. (*b*) Motor connections of a section of the simulated sandfish ($i = 1$ refers to the head). b indicates the width (maximum along the model) and height of the segments in the non-tapered section of the animal model. (*c*) Two representative contacting particles illustrating interaction forces given by equation (3.6). (*d*) Three-dimensional view of the 50 segment sandfish at three different instants while swimming within a container of particles rendered semi-transparent for visualization. The time for the simulated tapered head sandfish to swim across the container is approximately 3.5 s ($f = 2$ Hz). (*e*) Mid-line kinematics of subsurface sandfish motion in simulation when swimming at $f = 2.5$ Hz. (Online version in colour.)

RFT and the animal experiment. Then using each approach, we vary kinematic parameters to systematically test the RFT predictions as well as show an optimality condition for undulatory swimming in granular media.

4.1. Numerical sandfish simulation

The numerical simulation of the sandfish uses the commercial software package Working Model 2D (Design Simulation Technologies). The model is divided into 50 motor-actuated segments along its length (figure 3*a*). The angle of each motor is specified as a function of time such that an approximate sinusoidal wave travels posteriorly from head to tail (figure 3*b*). The angle (β_i) between segments i and $i+1$ varies as

$$\beta_i(t) = \tan^{-1}\left[\frac{2\pi A}{\lambda}\cos\left(\frac{2\pi}{l}x_{i+1} + 2\pi f t\right)\right] - \tan^{-1}\left[\frac{2\pi A}{\lambda}\cos\left(\frac{2\pi}{l}x_i + 2\pi f t\right)\right], \quad (4.1)$$

where x_i is the arc length measured from the tail tip to the i^{th} segment and l is the body length. To compare performance of the numerical simulation to the RFT, the morphology of the simulated animal is approximated as a square cross-section tube (figure 3*a*, inset).

The model does not incorporate limbs as the sandfish places its limbs along its sides during subsurface swimming (figure 1*b*). No tapering in height of the body along its length is considered, as doing so results in the model rising as it moves forward owing to drag-induced granular lift. This lift results from the vertical component of the normal force on an inclined surface dragged through a granular medium and is discussed in Ding *et al.* [50] and Maladen *et al.* [51].

We perform simulations for a square tube body shape, and to more closely match the animal we perform simulations using a model tapered in the coronal plane (figure 3*a*) with width varying linearly from the snout tip to 1/6 bl, and from 3/5 bl to the tail tip. Model properties such as animal dimensions and density are taken from biological measurements (refer to electronic supplementary material, table S1, for values). The segment height and maximum segment width are both denoted by b for the model. The body-particle friction ($\mu_{bp} = 0.27$) was determined by measuring the angle at which an anaesthetized sandfish slid snout-first down a monolayer of 3 mm glass particles glued to a flat plate [16]. For simplicity, we use the same normal force parameters for both the particle–particle and body–particle interactions.

The multi-segment model of the animal is combined with the previously described experimentally validated DEM simulation of the granular medium (in a container with comparable dimensions to those in experiment, see electronic supplemental material, table S1) such that Working Model integrates the equations of motion of the coupled links that represent the animal and the DEM calculates the resultant force from both the particle–particle and body–particle interactions. At each time-step, the net force from particles contacting each segment is passed to Working Model, and velocity and position information for each segment is transferred back to the DEM simulation. The animal model kinematics are constrained to prevent rotation of the axis of the travelling wave out of the horizontal plane of motion (roll).

With a flat head and square tubular body and using $A/\lambda = 0.22$ and $\xi = 1$ (from animal experiments), the simulated sandfish moves in loosely packed 3 mm particles with $\eta = 0.45$, while for the same shape, the RFT predicts $\eta = 0.66$. With the tapered sandfish body in simulation, the forward velocity of the simulation increases linearly with oscillation frequency, as in the animal experiments and the flat head and square tubular body simulation, and the slope of the relationship, $\eta = 0.57 \pm 0.01$ (figure 1*d*,*e*) is close to $\eta = 0.54 + 0.13$ observed for the animal. Accounting for tapering along the sandfish body in the RFT is complicated as the taper at the head and tail can become leading and trailing surfaces at different instances. This violates an RFT assumption that the net force can be decomposed into time-invariant body and head terms. We estimated the amount of head drag reduction owing to tapering as approximately 30 per cent (in accord with drag-reduction measurements [52]) by comparing the integrated drag force on the flat head to the tapered head in simulation. The RFT for the reduced head drag over-estimates the wave efficiency, predicting $\eta = 0.75$. We discuss potential reasons for the differences in η between simulation and RFT in §7.

4.2. Sandfish-inspired robot

To test the RFT and numerical simulation predictions in a real world environment, we built a physical model, a robot. Robots complement the theoretical and numerical modelling approaches because physical laws that govern the interaction with the granular medium need not be simulated.

The basic mechanical design of our robot is adapted from previously developed snake robots [53], which consist of modules (motors) with a single joint that permits angular excursions in the body plane and that are connected via identical links to form the body. Our design employs six standard size ($4 \times 3 \times 3.7\,\mathrm{cm}^3$) servomotors (Hitec, HSR 5980SG) and a passive segment (the head) with the same weight and form factor as a motor with its attached connectors for a total of seven segments. Each servomotor is powered in parallel from a 7.4 V, 30 A power supply. The pulse width-based control signal for each motor is generated using LabVIEW as a single analogue waveform initially determined from equation (4.2), output from a PCI-card (NI-6230) and transmitted via a multiplexer to each motor as control input.

Preliminary tests of the robot revealed that the kinematics prescribed by the sinusoidal travelling wave (equation (4.1)) are accurate only for low amplitudes because of the finite segment length associated with a finite number of segments (fixed total length). To obtain a larger range of amplitudes, we implemented an open loop controller that modulates the angle between adjacent segments using

$$\beta_i(t) = \beta_0 \xi \sin(2\pi\xi i/N - 2\pi f t), \tag{4.2}$$

where $\beta_i(t)$ is the angle between the i and $i+1$ motor at time t, β_0 is the angular amplitude, ξ is the number of wavelengths along the body (period) and N is the number of motors. We experimentally verified that the motors are able to achieve the prescribed joint excursions by observing the kinematics of the robot subsurface using X-ray imaging.

To reduce the motor torque requirements, we use 5.87 ± 0.06 mm plastic particles with particle density $= 1.03 \pm 0.04\,\mathrm{g\,cm}^{-3}$ as our granular medium (see electronic supplementary material, table S1, for details); we refer to these particles as '6 mm particles'. The granular bed is 110 cm × 40 cm and filled 14 cm deep. To prevent particles from intruding between motor segments and jamming the device, we encase the robot in a double-layer skin; a lycra spandex sleeve with a single seam (located at the top of the device) is slid over a snugly fitting elastic latex sleeve that prevents particles from getting between the motors during phases of the motion when the lycra sleeve is loose. The outer layer reduces the wear on the thin inner layer, allowing greater than 100 subsurface trials without replacement of the inner layer. The control and power wire bundle is run along the top of the motors (under the inner latex sleeve) to a mast on the last segment and is tethered above the container.

Overhead video (100 fps) is collected for each experiment. To track the subsurface position of the robot, a lightweight mast is attached to the first and last motor segment with a marker (visible above ground) (figure 4*a*,*e*). The kinematics of the subsurface motion

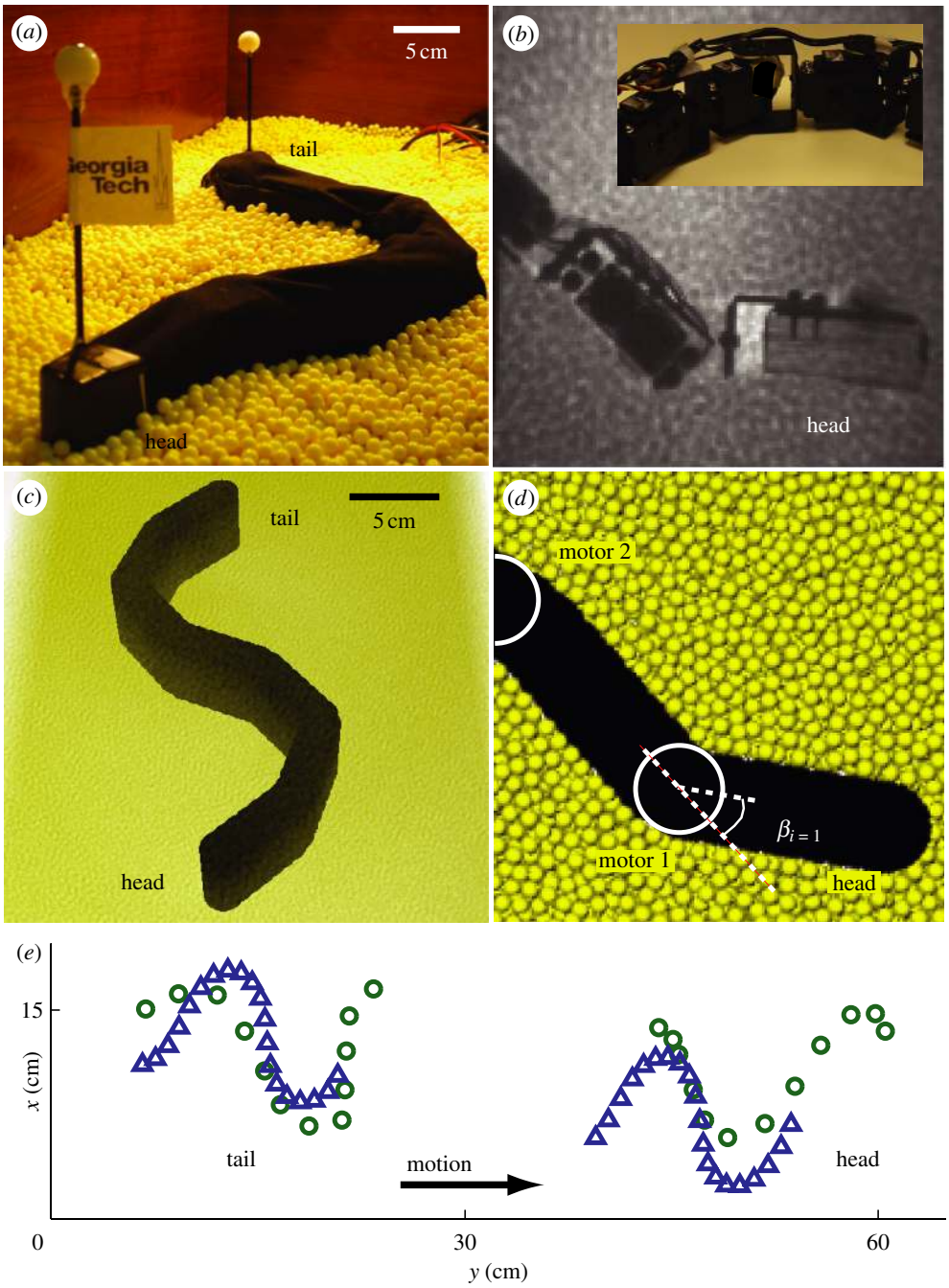

Figure 4. Robot model of the sandfish (*a*) resting in a container filled with 6 mm plastic particles and (*b*) swimming subsurface in the same particles (X-ray image). Inset in (*b*) shows the motors (segments) of the robot connected via c- and l-brackets without skin.(*c*) Three-dimensional rendering of the numerically simulated robot swimming in 6 mm particles. (*d*) Simulated robot showing the angle between adjacent segments (β_i) given by equation (4.2). (*e*) Circles in green and triangles in blue correspond to the tracked position of the head and tail segments of the robot as it swims subsurface in experiment and simulation, respectively. (Online version in colour.)

of the robot are also verified using X-ray video (figure 4*b*) for a representative condition. For each test, the robot is submerged 4 cm (from its top) into the medium and the surface is levelled and smoothed. At least 1.5 cycles of motion are collected for each trial (see electronic supplementary material, movie S3).

Like the sandfish lizard and the RFT and numerical simulation models, the forward velocity of the robot monotonically increases with increasing f (figure 5*a*) for $A/\lambda = 0.2$ and a single period wave. However, for the robot, $\eta = 0.34 \pm 0.03$, significantly below the values measured for the animal in experiment, and predicted by the RFT and animal numerical simulation.

We speculate that the η of the robot is less than that of the sandfish in biological experiment, RFT and numerical models because the small number of segments do not allow the robot to achieve a smooth sinusoidal profile. To investigate segment number effects, rather than increasing the number of motors in experiment, we adapt the numerical sandfish simulation to match the robot and its granular medium in physical dimension, mass and density (figure 4*c*).

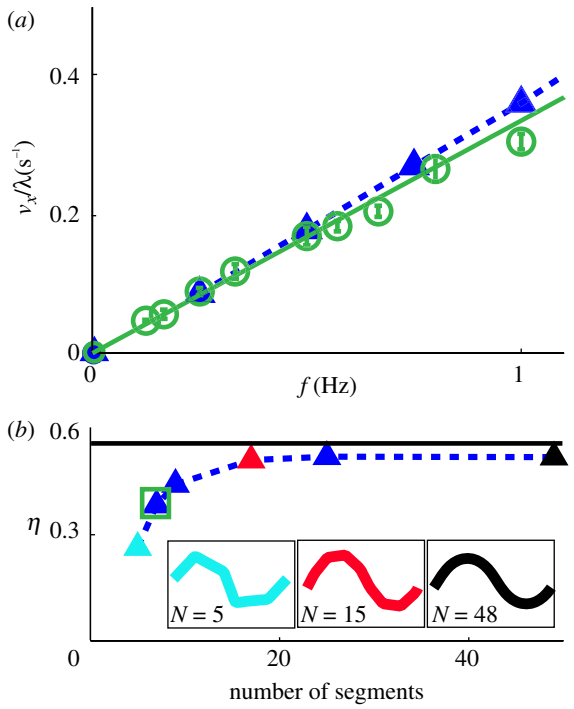

Figure 5. Comparison of robot experiment and simulation in 6 mm plastic particles. (*a*) Forward velocity increases linearly with undulation frequency in experiment (green open circles) and simulation (blue solid triangles). The slope of the dashed blue (simulation) and solid green (experiment) lines is the wave efficiency η with value 0.34 ± 0.03 in experiment and $\eta = 0.36 \pm 0.02$ in simulation. (*b*) η versus number of segments, N, for a fixed length robot plateaus at $N \approx 15$. The green box corresponds to the seven-segment robot in experiment while the horizontal black bar is the RFT prediction, $\eta = 0.56$ for a continuous robot body. Inset: schematics of 5-, 15- and 48-segment robots correspond to the η marked with similarly coloured (cyan, red and black) triangles. The robot simulation was tested at $f = 2$ Hz. For (*a*) and (*b*) $A/\lambda = 0.2$. We do not solve the RFT for the finite (7) segment robot as the resulting complex mathematical description provides less insight than the numerical simulation of the robot. (Online version in colour.)

We do this in simulation as increasing the number of motors experimentally is challenging: doing so would require an increased number of smaller motors with high torque requirements to maintain the same total length as the seven-segment robot.

The simulated robot, like the actual device, consists of seven segments and the angle between adjacent segments is modulated using equation (4.2). The robot model is tested in a validated granular medium consisting of a 50 : 50 bi-disperse mixture of 5.81 and 5.93 diameter particles; we will refer to this mixture as '6 mm plastic particles'. To validate the simulated medium and obtain the values of μ_{pp}, k and G_n given above, we dropped an aluminium ball (diameter 6.35 cm and mass 385 g) into the plastic particles with varying impact velocity (0.5–$3\ \mathrm{m\,s^{-1}}$) in both experiment and simulation and set grain interaction parameters to best match the measured and simulated penetration force during the impact collision as a function of time (see electronic supplementary material, figure S2 and table S1). With parameters determined from impact at $v = 1.4\ \mathrm{m\ s^{-1}}$, the force profile fits well at other impact velocities. In additional experiments, we directly measured the friction (particle–particle and particle–lycra skin) and restitution (particle–particle) coefficients for the plastic particles and found them to be within 5 and 10 per cent of the fitted values, respectively. The robot simulation results quantitatively match the robot experimental results (figure 5*a*) with velocity linear in f and $\eta = 0.36 \pm 0.02$ (see electronic supplementary material, movie S4).

Increasing N (for a fixed length device) in the robot simulation causes the robot to advance more rapidly and with greater η until $N \approx 15$, above which η remains constant at 0.54 (figure 5*b*), resulting in a performance comparable with that of the animal. η obtained from the RFT for a robot with a continuous profile (i.e. $N = \infty$) swimming in 6 mm plastic particles is nearly the same (black horizontal line, figure 5*b*). For the empirical force laws used in the RFT to predict η refer to electronic supplementary material, figure S4. For the smooth robot, the animal in 0.3 mm (loosely and closely packed media) [22] and 3 mm particles (§2), and in model predictions (§§3 and 4) in simulated 3 mm glass particles, the values of η are all close to 0.5. This suggests that subsurface locomotion in granular media is largely independent of media properties like particle size and density [51].

We postulate that η increases with increasing N because a smoother body profile facilitates media flow and leads to decreased drag and/or a decreased variation in the spatial form (A/λ) from the prescribed sinusoidal target (as much as 30% for $A/\lambda = 0.2$ with $N = 7$). Our finding that for $N > 15$, η saturates at a value close to that observed in the animal suggests that near-maximal performance occurs when the spatial form of the robot matches well a travelling sinusoidal wave.

5. VARIATION OF THE SINUSOIDAL KINEMATICS OF SAND-SWIMMING

To this point, we have limited our investigation of sand-swimming to parameters used by the sandfish, i.e. a sinusoidal travelling wave with fixed kinematics ($A/\lambda \approx 0.2$ and $\xi = 1$). We now use each of our three models to investigate how swimming depends on variation of the spatial form of the sinusoidal wave. This allows us to systematically test our models and to advance an argument for why the rapidly escaping animal uses only a limited range of A, λ and ξ.

We first discuss the RFT prediction of η for a fixed length sandfish model at fixed period ($\xi = 1$) with varying wave amplitude such that $0 < A/\lambda < 0.6$ (figure 6*a*). Solving equation (3.5) numerically reveals that η increases monotonically with increasing A/λ: slowly for small A/λ, rapidly for intermediate A/λ and slowly towards a plateau for large A/λ.

We compare the functional form of η versus A/λ from the RFT to the results from the numerical model with both constant and tapered cross section (figure 6*a*) and find that while the shape of the curves are similar, the RFT predictions (for the square cross section and for the reduced head drag) systematically overestimate η. However, scaling the net force (equation (3.1)) on each element (excluding the head) by a factor of 0.5

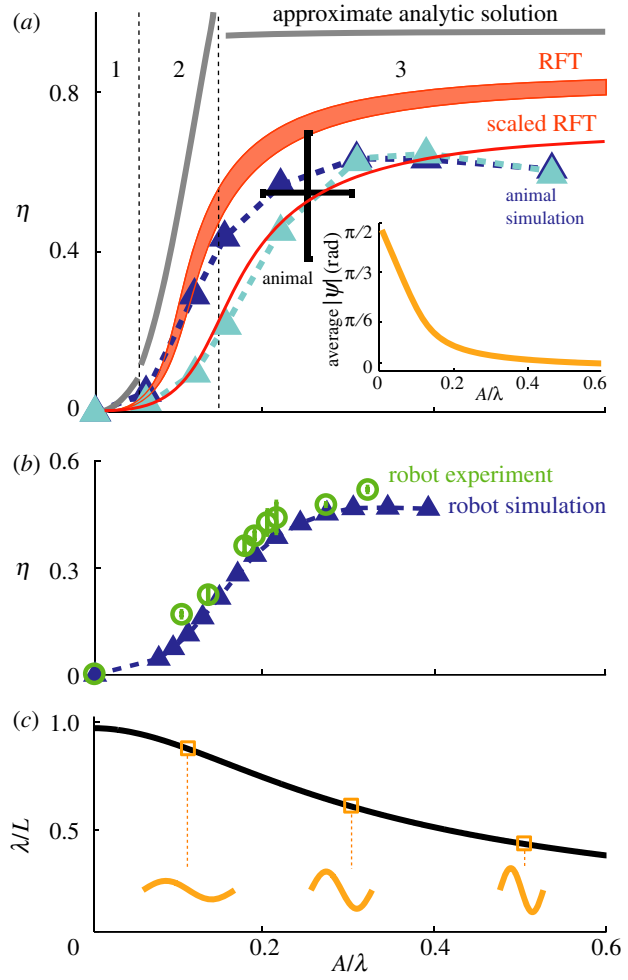

Figure 6. Sand swimming performance dependence on wave parameters. Wave efficiency η versus amplitude to wavelength ratio A/λ for (a) the numerical sandfish simulation (dashed curve and triangles, $f = 4$ Hz) with a tapered (dark blue) and uniform (cyan) square cross-section body. The pink shaded region corresponds to the RFT prediction for square cross-section body for maximum (flat plate, lower bound) and 30% of the maximum head drag (higher bound), respectively. The black cross corresponds to the animal experiments ($A/\lambda = 0.25 \pm 0.07$, $\eta = 0.53 \pm 0.16$). Grey solid curves correspond to the approximate analytical RFT solutions, and are divided into regions 1, 2 and 3 by dashed black vertical lines (regions correspond to those marked in figure 2b,c). The red curve is the RFT prediction of η for a square cross-section body with maximum head drag with the net force on each element scaled by 0.5 (see text). Inset: the average of the absolute value of ψ decreases with A/λ. (b) η versus A/λ for the robot experiment (green circles) and robot simulation (blue triangles and dashed curve), $f = 0.5$ Hz. (c) For a fixed length undulator, the wavelength decreases with increasing amplitude. Spatial forms are depicted by orange curves.

in the RFT prediction results in a curve that closely matches the non-tapered simulation (figure 6a). We return to this point in §7. For all A/λ, the simulated sandfish with tapered body progresses with a higher η than for the non-tapered sandfish mainly owing to the reduction in head drag. The dependence of η on A/λ from both robot experiment and simulation (figure 6b) qualitatively matches that predicted by the RFT and numerical sandfish simulation. As explained in §4.2, the reduced performance of the robot compared with the RFT and numerical sandfish simulation is due to the smoother body profile of the animal model (because of the larger number of segments) when compared with the robot.

5.1. *Analytical approximate solution for resistive force theory*

Since the shapes of the η versus A/λ curves are similar over a wide range of experimental and model conditions, and since performance limits on sand-swimming are determined by the dependence of η on A/λ, it is important to understand how parameters in the model affect this functional relationship. Therefore, we gain insight into this function by developing analytical solutions of the RFT in three regions: low A/λ, where η increases with positive curvature, intermediate A/λ, where η increases significantly and high A/λ, where η is largely independent of A/λ.

As equation (3.1) shows, thrust is determined by the orientation θ of the element, the maximum value of which increases with A/λ, and the magnitude of the normal force. The increase in the projected area of the element perpendicular to the forward motion of the animal (which increases thrust) explains the increase in η as a function of A/λ. Understanding the form of η versus A/λ in the three regions, however, requires examination of the measured force laws (figure 2b,c). Because of the non-trivial dependence of the force on ψ, we divide the η versus A/λ relationship into three adjacent regions (figure 6a) in each of which we approximate the force as either constant or linearly dependent on ψ. Below, we give a summary of the calculations; see electronic supplementary material for full details.

The order of the regions in figures 2 and 6 is reversed because A/λ and ψ are inversely related (inset, figure 6a). As solving the RFT numerically without head drag does not qualitatively affect the dependence of η on A/λ, we neglect head drag to simplify the analysis.

Region 1 (small A/λ). For small and increasing oscillation amplitude (and similarly for A/λ and θ), η increases from zero with an increasing rate. In this region as ψ decreases, the displacement of an element of the body of the animal remains nearly perpendicular to its forward velocity $\psi \approx \pi/2$ (figure 2b,c) for a majority of the cycle resulting in $F_\perp$ remaining nearly constant (at its maximum) while $F_\parallel$ increases. Consequently, the stresses perpendicular and parallel to an element can be approximated as:

$$\left.\begin{aligned} P_\perp &= \frac{F_\perp}{bd} = C^1_{S\perp}, \\ \text{and} \qquad P_\parallel &= \frac{F_\parallel}{bd} = C^1_\parallel(\pi/2 - \psi), \end{aligned}\right\} \tag{5.1}$$

where b and d correspond to the height and length of the element dragged through the medium. $C^1_{S\perp}$ and $C^1_\parallel$ are fitting parameters for the forces in Region 1 (values of the coefficients are given in electronic supplementary material, table S2). To derive an analytical solution in this region, we examine the numerical solution in figure 6 and find that in this region $\eta \approx 0$, $\theta \approx 0$ and $\psi \approx \pi/2$. Using these approximations and equation (5.1),

we solve for η in equation (3.5):

$$\eta = 2\pi^2 \left(\frac{C^1_{S\perp}}{C^1_{\parallel}} - 1 \right) \left(\frac{A}{\lambda} \right)^2. \tag{5.2}$$

In this region of small A/λ (or small η), as A/λ increases, $F_\perp/F_\parallel$ decreases rapidly, which competes with increasing $\sin\theta$ and results in the quadratic dependence of η on A/λ.

Region 2 (intermediate A/λ). For $0.05 < A/\lambda < 0.15$, η increases substantially and rapidly. In this region as ψ decreases $F_\perp$ increases slowly and $F_\parallel$ is nearly constant:

$$\left.\begin{aligned} P_\perp &= \frac{F_\perp}{bd} = C^2_{S\perp} + C^2_\perp \psi \\ \text{and} \qquad P_\parallel &= \frac{F_\parallel}{bd} = C^2_{S\parallel}, \end{aligned}\right\} \tag{5.3}$$

where $C^2_\perp$, $C^2_{S\perp}$ and $C^2_{S\parallel}$ are fitting parameters for the forces in Region 2. Solving for η gives

$$\eta = \left[\frac{C^2_{S\parallel} - 4C^2_{S\perp}\frac{A}{\lambda}}{16C^2_\perp \left(\frac{A}{\lambda}\right)^2} + 1 \right]^{-1}. \tag{5.4}$$

Physically, since $F_\perp/F_\parallel$ decreases slowly, η in this region is more sensitive to variations in $\sin\theta$, and therefore for increasing amplitude η increases rapidly and approximately linearly.

Region 3 (large A/λ). For increasing $A/\lambda > 0.15$, η increases slowly. Here, as ψ decreases, $F_\perp$ decreases rapidly while $F_\parallel$ saturates at its maximum as the sides of the dragged rod are nearly parallel to its velocity for a majority of each cycle. This gives

$$\left.\begin{aligned} P_\perp &= \frac{F_\perp}{bd} = C^3_\perp \psi, \\ \text{and} \qquad P_\parallel &= \frac{F_\parallel}{bd} = C^3_{S\parallel} + C^3_\parallel \psi, \end{aligned}\right\} \tag{5.5}$$

where $C^3_\perp$, $C^3_{S\perp}$ and $C^3_{S\parallel}$ are fitting parameters for the forces in Region 3. To derive an analytical solution, we assume $\eta \approx 1$, $\theta \approx \pi/2$ and $\psi \approx 0$ which gives,

$$\eta = 1 - \frac{4C^3_{S\parallel}}{4C^3_\perp - C^3_\parallel (A/\lambda)^{-1}}. \tag{5.6}$$

Physically, the decrease in $F_\perp/F_\parallel$ competes with the increase of $\sin\theta$ which plateaus for large amplitude (as θ approaches $\pi/2$), which causes η to increase slowly.

Overall, the analytical solution of the RFT correctly predicts that η increases quadratically for small A/λ, increases rapidly for intermediate A/λ and is nearly constant for large A/λ. For each region, the analytical form of η qualitatively agrees with the calculated shape of the η versus A/λ relationship (figure 6*a*). The analytic solutions demonstrate that the difference between swimming in sand and swimming in a low-*Re* Newtonian fluid is predominantly because of the difference in the functional forms of $F_\perp$ and $F_\parallel$ in these two media (in addition to the difference that in granular media, forces are speed independent for low speeds, <40 cm s^{-1} in our study). In low-*Re* fluids [39], $F_\perp$ and $F_\parallel$ are proportional to their respective projected velocities with coefficients in the ratio of 2 : 1. In contrast, in granular media, the functional forms of $F_\perp$ and $F_\parallel$ are more complicated and thus the effective coefficient ratio depends on A/λ. The larger slope of $F_\perp$ at smaller ψ (small A/λ) is largely responsible for the increased magnitude of η in granular media relative to that in low-*Re* swimmers like nematodes.

6. OPTIMAL SAND-SWIMMING

All our models predict that the animal increases η by increasing A/λ (figure 6*a*,*b*), but we find that the animal does not operate at high A/λ. Maladen *et al.* [22] showed using the RFT model that locomotion at large A/λ (figure 6*c*) comes with a cost: since the animal is of finite length, the distance it travels per cycle decreases with increasing A/λ. We can see this by expressing body lengths travelled per cycle as $v_x/fL = \eta\lambda/L$, as $v_x = \eta f\lambda$. While η increases with increasing A/λ, λ decreases and thus a maximum in forward progress per cycle can be expected. Figure 7*a*,*b* shows that as predicted by the RFT, both the numerical sandfish model and the physical and simulated robot models display a maximum forward progress per cycle at $A/\lambda \approx 0.2$. As expected, the simulated sandfish with a tapered body shape moves faster than the square-tube shape but the values of A/λ that maximize their forward speed are close (figure 7*a*). Similar to the prediction of η versus A/λ, the RFT systematically over-predicts the speed per cycle compared with the numerical simulation, but scaling the net force on each segment (effectively the thrust) by 0.5 in the RFT results in an excellent match between the RFT and numerical simulation of the square tube body. The biological data reside close to the peak of the curve, indicating that the animal is maximizing its sand-swimming speed. This result agrees with the hypothesis that sandfish burial is an escape response [28].

To test the effect of the number of wave periods on performance, we fixed $A/\lambda = 0.2$ and varied $0.3 < \xi < 1.6$. Testing was possible over only a limited range for the physical robot because for $\xi < 0.6$, the side walls of the test container interfere with the motion owing to large yawing of the robot and for $\xi > 1.3$, the maximum angle required to maintain $A/\lambda = 0.2$ exceeds the range of motion of the servos. The models progress forward fastest for approximately a single period along the body (figure 7*c*,*d*). The animal, as mentioned, operates close to the maximum speed predicted by the models.

We can explain the dependence of speed on ξ: for non-integer ξ the sandfish model experiences an unbalanced torque that results in a periodic yawing motion (with an amplitude of more than 40° for $\xi = 0.5$), which causes A to become effectively smaller and thus results in lower η. For fixed A/λ, as ξ increases λ decreases owing to the fixed body length. For $\xi < 1$, as ξ increases both yaw and λ decrease which has competing opposite effects on forward velocity and results in a maximum v_x at $\xi < 1$. For $\xi > 1$, as ξ increases, decreased v_x mainly results from the decrease in λ. We use the RFT to predict η only for a single period ($\xi = 1$) because determining η

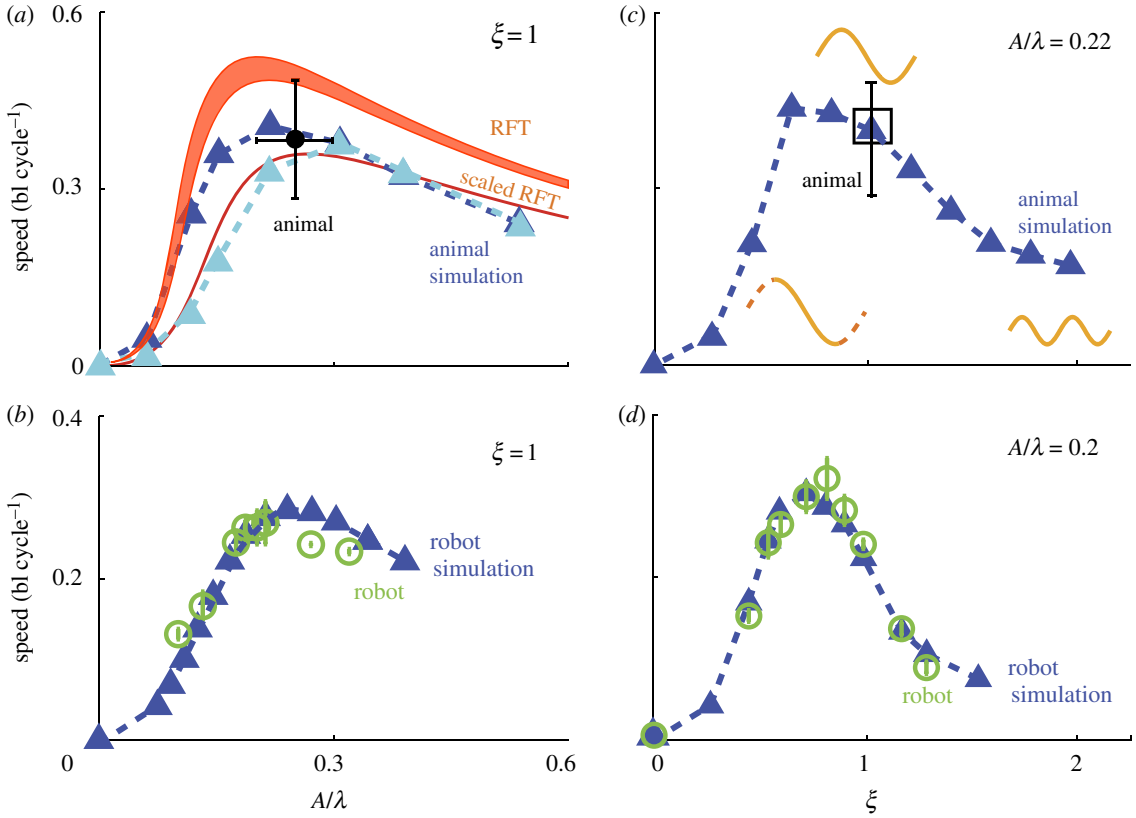

Figure 7. Kinematics that maximize swimming speed. (*a*) Forward speed (in bl per cycle) measured while varying the ratio of A to λ for a single period wave. The cyan and blue dashed curves with triangles correspond to the sandfish simulation with flat and tapered heads, respectively. A third order polynomial fit to the peak of the tapered head sandfish simulation curve in identifies the maximum speed $= 0.41 \pm 0.01$ bl cycle^{-1} at $A/\lambda = 0.23 \pm 0.01$. The pink shaded region corresponds to the RFT prediction for square cross-section body for maximum (flat plate, lower bound) and 30% of the maximum (higher bound) head drag, maximum swimming speeds correspond to $A/\lambda = 0.19$ and $A/\lambda = 0.21$, respectively. The red curve is the RFT prediction of forward speed for a square cross-section body with maximum head drag with the net force on each element scaled by 0.5 (see text). The maximum forward speed corresponds to $A/\lambda = 0.27$. (*b*) Forward speed for the robot in experiment (green circles) and simulation (dashed blue curve with triangles) corresponding to varying A/λ (with $\xi = 1$). Fitting the peak of the robot simulation curve with a third order polynomial identifies the maximum speed $= 0.28 \pm 0.01$ bl cycle^{-1} at $A/\lambda = 0.24 \pm 0.01$. (*c*) Forward speed measured while varying ξ in the sandfish model with $A/\lambda = 0.22$. Spatial forms depicted by orange curves. (*d*) Forward speed for the robot in experiment (green circles) and simulation (dashed blue curve with triangles) corresponding to varying ξ (with $A/\lambda = 0.2$). For the numerical sandfish results (*a*,*c*) $f = 2$ Hz and for the robot experiment and simulation results (*b*,*d*) $f = 0.5$ Hz. Black cross ($A/\lambda = 0.25 \pm 0.07$, speed $= 0.39 \pm 0.1$ bl cycle^{-1}) in (*a*) and black box ($\xi = 1$) in (*c*) correspond to measurements from animal experiment.

for non-integer ξ is challenging owing to unbalanced torques in the plane of motion.

7. DISCUSSION AND CONCLUSION

Motivated by biological experiments of sandfish locomotion, we developed numerical modelling and robotic approaches to study undulatory sand-swimming. We used the models to test the predictions of our previously developed empirical resistive force model and demonstrated that limbless undulatory locomotion with η comparable with that of the animal can be achieved within granular media by models using the wave kinematics of the animal. We determined how η depends on amplitude and developed approximate analytical solutions that give insight into how the interdependent effects of thrust and drag forces, orientation of body elements and spatial characteristics of the animal influence η. With each model, we showed that the competing effects of wave efficiency and wavelength determine forward speed, and that $A/\lambda \approx 0.2$ and $\xi \approx 1$ maximize forward swimming speed. The sandfish uses these optimal kinematics to swim rapidly within granular media. The performance measured in experiment and predicted by each model obtained by constraining only kinematics (and not forces) was the same as that of the animal across a range of media properties like particle size and density.

The RFT over-predicts η for varying A/λ but the agreement of the functional form of the relationship compared with the non-tapered simulation is good. The cause of these performance differences may lie in the assumptions of the RFT. First, at larger A/λ, the assumption that the forces associated with each element are localized may be inaccurate. As the amplitude increases, the region of particles influenced by the adjacent segments may overlap, which could cause a reduction in thrust and thus performance.

Second, the force on the body of the model sandfish is different for the RFT and the numerical simulation. The net force on the body is nearly 50 per cent lower

(for $A/\lambda = 0.22$) in simulation than estimated by the RFT because a segment decelerates as it reaches its maximum lateral excursion (A) and accelerates after the velocity direction reverses. This results in a varying velocity and a possible hysteresis effect as the lateral displacement reverses, which are not considered in the RFT. Hence, the deviation from the constant steady state velocity assumption of the RFT may be responsible for the over-prediction in η when compared with the numerical simulation for the η versus A/λ relation (figure 6*a*).

Third, an effect of possible importance at higher A/λ is that while the centre of mass (CoM) in both animal and numerical simulation oscillate laterally during locomotion, the RFT assumes that the CoM does not oscillate. Lateral CoM oscillation reduces the effective amplitude and changes the effective orientation (ψ) of each element which, according to our force measurements, should decrease η. Also yaw motion is not considered in the RFT.

Future comparison of the models will elucidate contributions from these three mechanisms and thus allow for better understanding of the physics of forces in granular media. With advances in our understanding of force generation in granular media, the RFT will be improved, potentially allowing it to accurately predict η for more complicated geometries such as the smoothly tapered body of the sandfish or the more discretized shape of the robot.

We now discuss the assumption of planar motion used throughout our modelling. Although the sandfish swims into the medium at angles between 20° and 30° relative to the horizontal, the RFT assumes that locomotion occurs in a horizontal plane; comparison with the numerical simulation and physical robot is made for the same horizontal orientation. Previous calculations showed that since resistive forces increase linearly with depth [47,48], the net thrust and drag generated by the body of the animal are unaffected by the entry angle. This suggests that the dominant effect of an angled swim is an increase in head drag. Based on measurements from side view X-ray data of the animal [22], we estimate that the force per area on the head is 1.5 times larger than on the centre of the body. With increased head drag, the RFT predicts that η at 22° should be approximately 15 per cent smaller than that for horizontal swimming. Simulation of a sandfish model constrained in a plane at 22° relative to the horizontal plane shows that swimming speed is approximately 16 per cent slower than in the horizontal case. This finding supports our RFT prediction that the dominant effect of swimming at an angle is an increase in head drag. The fact that the η predicted by the numerical model for the tapered body is higher (swimming at a fixed depth) (figure 1*e*) than that measured for the animal (swimming at 22°) is consistent with the increase in head drag for angled dives.

Our complementary modelling techniques have individual strengths and weaknesses. For example, while RFT can be rapidly solved to predict organism performance, predictions in different media and with different preparation require re-determination of the empirical force laws, which is inconvenient. In contrast, although the numerical simulation is slower (several days on a desktop PC), the experimentally validated simulation can give an understanding of these force interactions from the particle perspective and can be used to generate empirical drag laws for input into RFT. The simulation is also a flexible design tool with which parameters like particle–particle friction and animal kinematics can be easily varied to accurately predict performance. The robot is a key complement to the numerical and theoretical approaches as it validates predictions in a real world environment. However, unlike simulations, the robot is not amenable to extensive adjustments and cannot be used conveniently to measure particle forces and flowfields.

The framework of experimental visualization techniques, and theoretical, computational and physical modelling approaches that we have described here will allow us to develop and test mechanical hypothesis of interaction between the locomotor and its surroundings [54]. All models allow variation of parameters that are difficult to vary and control in organisms and can thus address questions concerning mechanical cost of transport, effect of body shape, skin friction, burial/unburial mechanics, manoeuvring, control methodologies [55], sensing and sand-swimming performance. These tools will also allow investigation of the detailed physics that governs the form of the force laws within granular media. The models can be used as design tools to develop the next generation of biophysically inspired sand-swimming robots that will explore complex flowing environments.

We thank Mateo Garcia for characterizing the granular media, and Sarah Steinmetz for help with the animal experiments. We thank Andrew Slatton and Daniel Cohen for their assistance with the numerical sandfish simulation, and we thank Kellar Autumn for helpful discussion. This work was supported by The Burroughs Wellcome Fund Career Award at the Scientific Interface, NSF Physics of Living Systems grant PHY-0749991, and the Army Research Laboratory (ARL) Micro Autonomous Systems and Technology (MAST) Collaborative Technology Alliance (CTA) under cooperative agreement number W911NF-08-2-0004.

REFERENCES

1 Drucker, E. & Lauder, G. 1999 Locomotor forces on a swimming fish: three-dimensional vortex wake dynamics quantified using digital particle image velocimetry. *J. Exp. Biol.* **202**, 2393–2412.

2 Nauen, J. & Lauder, G. 2002 Quantification of the wake of rainbow trout (*Oncorhynchus mykiss*) using three-dimensional stereoscopic digital particle image velocimetry. *J. Exp. Biol.* **205**, 3271–3279.

3 Hedenstrom, A., Van Griethuijsen, L., Rosén, M. & Spedding, G. 2006 Vortex wakes of birds: recent developments using digital particle image velocimetry in a wind tunnel. *Anim. Biol.* **56**, 535–549. (doi:10.1163/157075606778967856)

4 Fontaine, E., Zabala, F., Dickinson, M. & Burdick, J. 2009 Wing and body motion during flight initiation in *Drosophila* revealed by automated visual tracking. *J. Exp. Biol.* **212**, 1307–1323. (doi:10.1242/jeb.025379)

5 Bejan, A. & Marden, J. 2006 Unifying constructal theory for scale effects in running, swimming and flying. *J. Exp. Biol.* **209**, 238–248. (doi:10.1242/jeb.01974)

6 Holmes, P., Full, R. J., Koditschek, D. & Guckenheimer, J. 2006 The dynamics of legged locomotion: models, analyses, and challenges. *SIAM Rev.* **48**, 207–304. (doi:10.1137/S0036144504445133)
7 Lighthill, M. 1971 Large-amplitude elongated-body theory of fish locomotion. *Proc. R. Soc. Lond. B* **179**, 125–138. (doi:10.1098/rspb.1971.0085)
8 Mittal, R., Dong, H., Bozkurttas, M., Lauder, G. & Madden, P. 2006 Locomotion with flexible propulsors: II. Computational modeling of pectoral fin swimming in sunfish. *Bioinspiration Biomimet.* **1**, S35. (doi:10.1088/1748-3182/1/4/S05)
9 Shimada, T., Kadau, D., Shinbrot, T. & Herrmann, H. 2009 Swimming in granular media. *Phys. Rev. E* **80**, 020301. (doi:10.1103/PhysRevE.80.020301)
10 Eldredge, J. 2006 Numerical simulations of undulatory swimming at moderate Reynolds number. *Bioinspiration Biomimet.* **1**, S19–S24. (doi:10.1088/1748-3182/1/4/S03)
11 Crespi, A. & Ijspeert, A. 2008 Online optimization of swimming and crawling in an amphibious snake robot. *IEEE Trans. Robot.* **24**, 75–87. (doi:10.1109/TRO.2008.915426)
12 Kato, N. & Kamimura, S. 2007 *Bio-mechanisms of swimming and flying: fluid dynamics, biomimetic robots, and sports science*. Berlin, Germany: Springer.
13 Lehmann, F. 2004 Aerial locomotion in flies and robots: kinematic control and aerodynamics of oscillating wings. *Arthropod Struct. Dev.* **33**, 331–345. (doi:10.1016/j.asd.2004.05.003)
14 Ellington, C. 1999 The novel aerodynamics of insect flight: applications to micro-air vehicles. *J. Exp. Biol.* **202**, 3439–3448.
15 Dabiri, J. & Gharib, M. 2005 The role of optimal vortex formation in biological fluid transport. *Proc. R. Soc. B* **272**, 1557–1560. (doi:10.1098/rspb.2005.3109)
16 Hu, D., Nirody, J., Scott, T. & Shelley, M. 2009 The mechanics of slithering locomotion. *Proc. Natl Acad. Sci. USA* **106**, 10 081–10 085. (doi:10.1073/pnas.081 2533106)
17 Tytell, E., Hsu, C., Williams, T., Cohen, A. & Fauci, L. 2010 Interactions between internal forces, body stiffness, and fluid environment in a neuromechanical model of lamprey swimming. *Proc. Natl Acad. Sci. USA* **107**, 19 832–19 837. (doi:10.1073/pnas.1011564107)
18 Biewener, A. 1990 Biomechanics of mammalian terrestrial locomotion. *Science* **250**, 1097–1103. (doi:10.1126/science.2251499)
19 Vogel, S. 1996 *Life in moving fluids: the physical biology of flow*. Princeton, NJ: Princeton University Press.
20 Alexander, R. 2003 *Principles of animal locomotion*. Princeton, NJ: Princeton University Press.
21 Cohen, N. & Boyle, J. 2009 Swimming at low Reynolds number: a beginners guide to undulatory locomotion. *Contemp. Phys.* **51**, 103–123. (doi:10.1080/00107510903268381)
22 Maladen, R., Ding, Y., Li, C. & Goldman, D. 2009 Undulatory swimming in sand: subsurface locomotion of the sandfish lizard. *Science* **325**, 314–318. (doi:10.1126/science.1172490)
23 Dorgan, K., Arwade, S. & Jumars, P. 2007 Burrowing in marine muds by crack propagation: kinematics and forces. *J. Exp. Biol.* **210**, 4198–4212. (doi:10.1242/jeb.010371)
24 Guo, Z. & Mahadevan, L. 2008 Limbless undulatory propulsion on land. *Proc. Natl Acad. Sci. USA* **105**, 3179–3184. (doi:10.1073/pnas.0705442105)
25 Norris, K. & Kavanau, J. 1966 The burrowing of the western shovel-nosed snake, *Chionactis occipitalis* Hallowell, and the undersand environment. *Copeia* **1966**, 650–664. (doi:10.2307/1441397)
26 Tritton, D. 1989 *Physical fluid dynamics*. Oxford, UK: Oxford University Press.
27 Anderson, J. & Wendt, J. 1995 *Computational fluid dynamics*. New York, NY: McGraw-Hill.
28 Arnold, E. 1995 Identifying the effects of history on adaptation: origins of different sand-diving techniques in lizards. *J. Zool. Lond.* **235**, 351–388. (doi:10.1111/j.1469-7998.1995.tb01758.x)
29 Gaymer, R. 1971 New method of locomotion in limbless terrestrial vertebrates. *Nature* **234**, 150–151. (doi:10.1038/234150a0)
30 Gasc, J., Jouffroy, F., Renous, S. & Von Blottnitz, F. 2009 Morphofunctional study of the digging system of the Namib Desert golden mole (*Eremitalpa granti namibensis*): cinefluorographical and anatomical analysis. *J. Zool.* **208**, 9–35. (doi:10.1111/j.1469-7998.1986.tb04706.x)
31 Mosauer, W. 1932 Adaptive convergence in the sand reptiles of the Sahara and of California: a study in structure and behavior. *Copeia* **2**, 72–78. (doi:10.2307/1435888)
32 Russell, A. & Bels, V. 2001 Biomechanics and kinematics of limb-based locomotion in lizards: review, synthesis and prospectus. *Comp. Biochem. Physiol., Part A* **131**, 89–112.
33 Gans, C. 1988 Adaptation and the form-function relation. *Integr. Comp. Biol.* **28**, 681–697. (doi:10.1093/icb/28.2.681)
34 Gans, C. 1975 Tetrapod limblessness: evolution and functional corollaries. *Integr. Comp. Biol.* **15**, 455–467. (doi:10.1093/icb/15.2.455)
35 Calcott, B. 2009 Lineage explanations: explaining how biological mechanisms change. *Br. J. Phil. Sci.* **60**, 51–78. (doi:10.1093/bjps/axn047)
36 Lamb, T. & Bauer, A. 2006 Footprints in the sand: independent reduction of subdigital lamellae in the Namib–Kalahari burrowing geckos. *Proc. R. Soc. B* **273**, 855–864. (doi:10.1098/rspb.2005.3390)
37 Bagnold, R. A. 1954 *The physics of blown sand and desert dunes*. MA, USA: Methuen and Co. Ltd.
38 Li, C., Umbanhowar, P. B., Komsuoglu, H., Koditschek, D. E. & Goldman, D. I. 2009 Sensitive dependence of the motion of a legged robot on granular media. *Proc. Natl Acad. Sci. USA* **106**, 3029–3034. (doi:10.1073/pnas.0809095106)
39 Gray, J. & Hancock, G. 1955 The propulsion of sea-urchin spermatozoa. *J. Exp. Biol.* **32**, 802–814.
40 Rapaport, D. 2004 *The art of molecular dynamics simulation*. Cambridge, UK: Cambridge University Press.
41 Nedderman, R. 1992 *Statics and kinematics of granular materials*. Cambridge, UK: Cambridge University Press.
42 Bagnold, R. A. 1954 Experiments on a gravity-free dispersion of large solid spheres in a Newtonian fluid under shear. *Proc. R. Soc. Lond. A* **225**, 49–63. (doi:10.1098/rspa.1954.0186)
43 McDonald, J. 2008 *Handbook of biological statistics*. Baltimore, MD: Sparky House.
44 Gray, J. & Lissmann, H. 1964 The locomotion of nematodes. *J. Exp. Biol.* **41**, 135–154
45 Jayne, B. 1986 Kinematics of terrestrial snake locomotion. *Copeia* **1986**, 915–927. (doi:10.2307/1445288)
46 Gray, J. 1946 The mechanism of locomotion in snakes. *J. Exp. Biol.* **23**, 101–120.
47 Albert, R., Pfeifer, M. A., Barabasi, A. L. & Schiffer, P. 1999 Slow drag in a granular medium. *Phys. Rev. Lett.* **82**, 205–208. (doi:10.1103/PhysRevLett.82.205)
48 Wieghardt, K. 1975 Experiments in granular flow. *Ann. Rev. Fluid Mech.* **7**, 89–114. (doi:10.1146/annurev.fl.07.010175.000513)
49 Lee, J. & Herrmann, H. 1993 Angle of repose and angle of marginal stability: molecular dynamics of granular

particles. *J. Phys. A: Math. Gen.* **26**, 373–383. (doi:10.1088/0305-4470/26/2/021)

50 Ding, Y., Gravish, N. & Goldman, D. I. 2011 Drag induced lift in granular media. *Phys. Rev. Lett.* **106**, 028001. (doi:10.1103/PhysRevLett.106.028001)

51 Maladen, R., Ding, Y., Umbanhowar, P. & Goldman, D. In press. Undulatory swimming in sand: experimental and simulation studies of a robotic sandfish. *Int. J. Robot. Res.*

52 Albert, I., Sample, J., Morss, A., Rajagopalan, S., Barabási, A. & Schiffer, P. 2001 Granular drag on a discrete object: shape effects on jamming. *Phys. Rev. E* **64**, 61 303. (doi:10.1103/PhysRevE.64.061303)

53 Dowling, K. 1999 Limbless locomotion: learning to crawl. In *Proc. of IEEE Int. Conf. on Robot. Autom., Detroit, 1999*, vol. 4. IEEE.

54 Nishikawa, K. *et al.* 2007 Neuromechanics: an integrative approach for understanding motor control. *Integr. Comp. Biol.* **47**, 16–54. (doi:10.1093/icb/icm024)

55 Ijspeert, A., Crespi, A. & Cabelguen, J. 2005 Simulation and robotics studies of salamander locomotion. *Neuroinformatics* **3**, 171–195. (doi:10.1385/NI:3:3:171)

Electronic Supplementary Material: Mechanical models of sandfish locomotion reveal principles of high performance subsurface sand-swimming

Ryan D. Maladen[1], Yang Ding[2], Paul B. Umbanhowar[3], Adam Kamor[2], and Daniel I. Goldman,[2,1*]

[1]Interdisciplinary Bioengineering Program

[2]School of Physics, Georgia Institute of Technology,

Atlanta, GA 30332, USA

[3]Department of Mechanical Engineering, Northwestern University

Evanston, IL 60208, USA

[*]E-mail: daniel.goldman@physics.gatech.edu

Analytic approximate solution to the Resistive Force Model (RFT)

In this section we present a more detailed derivation of the approximate analytic forms of η vs. A/λ shown in figure 6 and discussed in §5 in the main paper. References to equations here correspond to the equations presented in this document, not in the main text.

We previously developed a Resistive Force Theory for sandfish locomotion in granular media (*1*) in which the animal is modeled as a flexible tube with a sinusoidal traveling wave progressing from head to tail (figure 2*a*) such that the displacement of the animal away from the straight midline is given by

$$y = A \sin \frac{2\pi}{\lambda}(x + v_w t), \tag{1}$$

where y is the displacement from the mid-line of a straight animal, A is the amplitude, λ is the wavelength, f is the wave frequency, $v_w = f\lambda$ is the wave speed, t is the time, and x is the distance along a line joining the ends of the animal and parallel to the direction of motion. We assume there is no lateral translation (y-direction) nor yaw motion of the entire body so y also represents the lateral position in the lab frame. For a given forward velocity v_x, additional

quantities characterizing the motion can be calculated:

$$v_y = \frac{dy}{dt} = \frac{2A\pi v_w}{\lambda} \cos \frac{2\pi}{\lambda}(x + v_w t) \tag{2}$$

$$\tan\theta = \frac{dy}{dx} = \frac{2A\pi}{\lambda} \cos \frac{2\pi}{\lambda}(x + v_w t) \tag{3}$$

$$\psi = \tan^{-1}\left(\frac{v_y}{v_x}\right) - \theta, \tag{4}$$

where v_y is the y-component of the velocity, θ is the angle of the axis of an infinitesimal element with respect to the forward direction and ψ is the angle between the axis of the element and its instantaneous velocity. The wave efficiency η is defined as the ratio of the forward body speed to the traveling wave speed: $\eta = v_x/v_w$.

We assume that the forces $F_\perp$ and $F_\parallel$ (see figure 2*a* for the force diagram, and §3 of the text for a discussion of the force model) on an infinitesimal element of the animal are functions of only ψ and are proportional to the area of the longitudinal cross section bds, where b is the height of the element and $ds = \sqrt{1 + \tan^2\theta}dx$ is the arc length. By integrating the force over the body and accounting for the head drag F_{hx}, the resultant average net force in the forward direction (+x-direction) is:

$$\bar{F}_x = \int_0^\lambda (P_\perp \sin\theta - P_\parallel \cos\theta)\sqrt{1 + \tan^2\theta} b dx + \bar{F}_{hx}, \tag{5}$$

where $P_\perp$ and $P_\parallel$ are stresses perpendicular and parallel to the axis of each infinitesimal element and $\bar{F}_{hx}$ is the cycle averaged head drag. By assuming a constant forward average velocity (net forward force along the body equal to zero), the speed of the organism and thus the wave efficiency η can be determined numerically.

To better understand the dependence of η on A/λ (figure 6*a*), we construct analytic solutions in three regions: low A/λ where η increases with positive curvature, intermediate A/λ where η increases rapidly, and high A/λ where η is approximately independent of A/λ. This analysis requires examination of the empirically determined drag force on a rod as a function of ψ (figure 2*b,c*) in the three regions (figure 6*a*) (see text for details). We neglect the head drag as it does not affect the shape of the curve and simplifies the analysis. We approximate $P_\perp$ and $P_\parallel$ as piece-wise linear functions of ψ. Approximation techniques are then used to obtain simpler analytical solutions.

Region 1

In Region 1, because the amplitude of undulation (A/λ) is small, θ is much less than unity (from equation (2)). Since the projection of the normal force (thrust) in the forward direction is small compared to the total force, the forward speed and hence the wave efficiency is small.

Also ψ is close to $\pi/2$ for most of each cycle. Accordingly we use the approximations $\theta \approx 0$ and $\psi \approx \pi/2$.

Starting with the expression for ψ given in equation (4) and noting that $v_x/v_y = \tan\left[\pi/2 - \tan^{-1}(v_y/v_x)\right] \approx \pi/2 - \tan^{-1}(v_y/v_x)$ we approximate ψ as follows:

$$\begin{aligned}
\psi &= \tan^{-1}(v_y/v_x) - \theta \\
&\approx \pi/2 - v_x/v_y - \theta \\
&\approx \pi/2 - \frac{\eta v_w}{\frac{2\pi A v_w}{\lambda}\cos\frac{2\pi}{\lambda}(x+v_w t)} - \frac{2\pi A}{\lambda}\cos\frac{2\pi}{\lambda}(x+v_w t) \\
&= \pi/2 - \frac{\eta}{I} - I, \text{ where } I = \frac{2\pi A}{\lambda}\cos\frac{2\pi}{\lambda}(x+v_w t) \\
&= \pi/2 - I\left(1+\frac{\eta}{I^2}\right).
\end{aligned} \tag{6}$$

In Region 1 (main text, figure 2*b*,*c*), the force per unit cross sectional area is approximated as

$$\begin{aligned}
P_\perp &= \frac{F_\perp}{bd} = C^1_{S\perp} \\
P_\parallel &= \frac{F_\parallel}{bd} = C^1_\parallel(\pi/2 - \psi),
\end{aligned} \tag{7}$$

where b and d are the height and length of the rod, and $C^1_{S\perp}$ and $C^1_\parallel$ are region specific (indicated by the superscript) constants.

The integral of the net forward force from equation (5) becomes

$$\begin{aligned}
\bar{F}_x &\approx \int_0^\lambda \left[C^1_{S\perp} I - C^1_\parallel I\left(1+\frac{\eta}{I^2}\right)\right] b dx \\
&\approx \left[C^1_{S\perp}\tilde{I} - C^1_\parallel \tilde{I}\left(1+\frac{\eta}{\tilde{I}^2}\right)\right] b\lambda,
\end{aligned} \tag{8}$$

where we replace I and I^2 in the integral by their average values $\tilde{I} = \frac{1}{\lambda}\int_0^\lambda |I| dx = \frac{4A}{\lambda}$ and $\tilde{I}^2 = \frac{1}{\lambda}\int_0^\lambda I^2 dx = 2\pi^2(\frac{A}{\lambda})^2$. Applying the constant velocity condition $\bar{F}_x = 0$ allows us to solve for η:

$$\begin{aligned}
C^1_{S\perp}\tilde{I}\lambda &= C^1_\parallel \tilde{I}\lambda\left(1+\frac{\eta}{\tilde{I}^2}\right) \\
\eta &= \left(\frac{C^1_{S\perp}}{C^1_\parallel} - 1\right)\tilde{I}^2 \\
&= 2\pi^2\left(\frac{C^1_{S\perp}}{C^1_\parallel} - 1\right)\left(\frac{A}{\lambda}\right)^2.
\end{aligned} \tag{9}$$

Region 2

In this region, $\eta \approx 0.3$ and the magnitude of θ and ψ are neither close to 0 nor $\pi/2$. To analytically solve for η, a first order Taylor expansion of the tangent function is used though it is a relatively poor approximation (indicated with $*$).

$$\begin{aligned} \psi &= \tan^{-1}\frac{v_y}{v_x} - \theta \\ \psi &\approx \frac{v_y}{v_x} - I \qquad\qquad (*) \\ \psi &\approx (\eta^{-1} - 1)I. \end{aligned} \tag{10}$$

In Region 2 (figure 2*b*,*c*), the force per unit cross sectional area can be approximated as:

$$\begin{aligned} P_\perp &= \frac{F_\perp}{bd} = C_{S\perp}^2 + C_\perp^2 \psi \\ P_\parallel &= \frac{F_\parallel}{bd} = C_{S\parallel}^2. \end{aligned} \tag{11}$$

The integral of the net forward force becomes

$$\begin{aligned} \bar{F}_x &= \int_0^\lambda \left(P_\perp \sin\theta - P_\parallel \cos\theta\right) \sqrt{1+\tan^2\theta} b dx \\ &\approx \int_0^\lambda \left[\left(C_{S\perp}^2 + C_\perp^2\psi\right)|\sin\theta| - C_{S\parallel}^2\cos\theta\right] \sqrt{1+\tan^2\theta} b dx \\ &\approx \int_0^\lambda \left\{\left[C_{S\perp}^2 + C_\perp^2\left(\eta^{-1}-1\right)I\right]I - C_{S\parallel}^2\right\} \sqrt{1+\tan^2\theta} b dx \\ &\approx \left\{\left[C_{S\perp}^2 \frac{4A}{\lambda} + C_\perp^2\left(\eta^{-1}-1\right)\frac{16A^2}{\lambda^2}\right] - C_{S\parallel}^2\right\} bL, \end{aligned} \tag{12}$$

where we replace I in the integral by its average value $\tilde{I}$ and $L = \int_0^\lambda \sqrt{1+\tan^2\theta}dx$ is the length of the body. Applying the constant velocity condition $\bar{F}_x = 0$ allows us to solve for η:

$$\begin{aligned} C_{S\perp}^2 \frac{4A}{\lambda} + C_\perp^2\left(\frac{1}{\eta}-1\right)\frac{16A^2}{\lambda^2} &= C_{S\parallel}^2 \\ \eta &= \frac{1}{\frac{C_{S\parallel}^2 - 4C_{S\perp}^2\frac{A}{\lambda}}{16C_\perp^2\left(\frac{A}{\lambda}\right)^2} + 1}. \end{aligned} \tag{13}$$

Region 3

In this region $\eta \approx 0.7$, and since the amplitude of the undulation (A/λ) is large, $\theta \approx \pi/2$ and $\psi \approx 0$ for most of the cycle (see inset of figure 6*a* in main article). We use the approximations $\theta \approx \pi/2$ and $\psi \approx 0$.

Starting with the expression for θ given in equation (3) and noting that $\tan(\pi/2-\theta) \approx \pi/2-\theta = 1/\tan\theta$ we approximate θ as follows:

$$\begin{aligned} \tan\theta &= \frac{2\pi A}{\lambda}\cos\frac{2\pi}{\lambda}(x+v_w t) \\ \theta &\approx \pi/2 - \frac{1}{I}. \end{aligned} \tag{14}$$

Similarly with the use of the approximation

$$\tan^{-1}\frac{v_y}{v_x} \approx \frac{\pi}{2} - \frac{v_x}{v_y}, \tag{15}$$

we have

$$\begin{aligned} \psi &= \tan^{-1}\frac{v_y}{v_x} - \theta \\ \psi &\approx \left(\frac{\pi}{2} - \frac{v_x}{v_y}\right) - \left(\frac{\pi}{2} - \frac{1}{I}\right) \\ \psi &= \frac{1-\eta}{I}. \end{aligned} \tag{16}$$

In Region 3 (figure 2*b,c*), the force per unit cross sectional area can be approximated as:

$$\begin{aligned} P_\perp &= \frac{F_\perp}{bd} = C_\perp^3 \psi \\ P_\parallel &= \frac{F_\parallel}{bd} = C_{S\parallel}^3 + C_\parallel^3 \psi. \end{aligned} \tag{17}$$

The integral of the net forward force becomes

$$\begin{aligned} \bar{F}_x &= \int_0^\lambda \left(P_\perp \sin\theta - P_\parallel \cos\theta\right)\sqrt{1+\tan^2\theta}\, b dx \\ &= \int_0^\lambda \left[C_\perp^3 \psi \tan\theta\cos\theta - \left(C_{S\parallel}^3 + C_\parallel^3\psi\right)\cos\theta\right]\sqrt{1+\tan^2\theta}\, b dx \\ &= \int_0^\lambda \left\{C_\perp^3 I^{-1}(1-\eta) I\cos\theta - \left[C_{S\parallel}^3 + C_\parallel^3 \frac{1}{I}(1-\eta)\right]\cos\theta\right\}\sqrt{1+\tan^2\theta}\, b dx \\ &= \int_0^\lambda \left[(C_\perp^3 - C_\parallel^3 I^{-1})(1-\eta)\cos\theta - C_{S\parallel}^3\cos\theta\right]\sqrt{1+\tan^2\theta}\, b dx \\ &\approx \left[(C_\perp^3 - C_\parallel^3 \tilde{I}^{-1})(1-\eta)\cos\theta - C_{S\parallel}^3\cos\theta\right] bL. \end{aligned} \tag{18}$$

In the last step I is replaced in the integral by its average value $\tilde{I}$. Applying the constant velocity condition $\bar{F}_x = 0$ allows us to solve for η:

$$\begin{aligned} (C_\perp^3 - I^{-1}C_\parallel^3)(1-\eta) &= C_{S\parallel}^3 \\ \eta &= 1 - \frac{4C_{S\parallel}^3}{4C_\perp^3 - \left(\frac{A}{\lambda}\right)^{-1} C_\parallel^3}. \end{aligned} \tag{19}$$

The physical interpretation for each region is described in the paper in §5. Overall, the analytic solution of the RFT correctly predicts that η increases quadratically for small A/λ, increases rapidly for intermediate A/λ and varies slowly for large A/λ. For each region, the analytical form of η qualitatively agrees with the predicted shape of the η vs. A/λ relationship, see figure 6*a*. For values of the coefficients refer to table S2.

Fitting functions for $F_\perp$ and $F_\parallel$

The following fitting functions are used to obtain analytical expressions for $F_\perp$ and $F_\parallel$ as a function of ψ for the data shown in figures S3,S4 (and in figure 2 in the main text, although in that figure the fits are not shown):

$$\begin{aligned} F_\perp &= C_S \sin\beta_0 \\ F_\parallel &= [C_F \cos\psi + C_L(1-\sin\psi)], \end{aligned} \tag{20}$$

where $\tan\beta_0 = \gamma \sin\psi$. For the forces on the end caps, ψ is replaced by $\pi/2 - \psi$ since the surfaces of the end caps are perpendicular to the rod axis. See table S3 for the values of the fitting parameters C_S, C_F, C_L and γ.

References

1. Maladen, R., Ding, Y., Li, C. & Goldman, D. 2009 Undulatory Swimming in Sand: Subsurface Locomotion of the Sandfish Lizard. *Science*, **325**, 314-318. (doi:10.1126/science.1172490)

2. Goldman, D. & Umbanhowar, P. 2008 Scaling and dynamics of sphere and disk impact into granular media. *Phys. Rev. E*, **77**, 21308. (doi:10.1103/PhysRevE.77.021308(14))

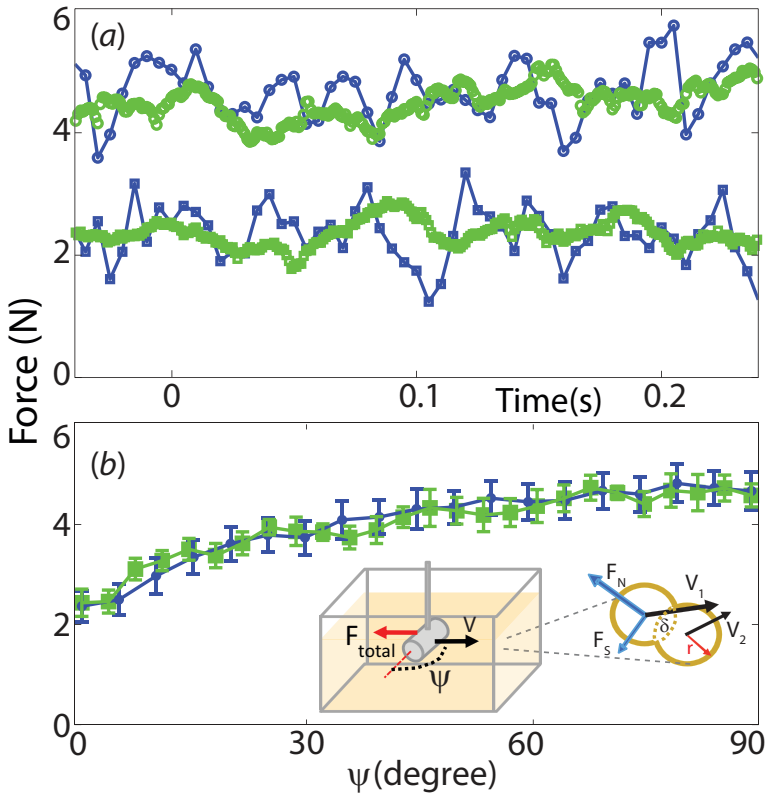

Figure S1: Validating the granular medium simulation for 3 mm glass spheres using rod drag experiments. Total force on a cylindrical rod (diameter $= 15.8$ mm, length $= 40$ mm) immersed to a depth of 7.6 cm in experiment (green) and simulation (blue) in a loosely packed medium. (a) Total force as a function of time in steady state region at two representative angles: $\psi = 0°$ (square) and $\psi = 90°$ (circle). (b) Average total force vs. ψ, the angle between the velocity and orientation of the rod. Inset shows the experimental setup and forces on two representative contacting particles whose interaction forces are given by equation (6) in the main text. Parameters for the numerical simulation are given in table S1 except for μ_{bp}. $\mu_{bp} = 0.15$ was used to match the friction coefficient between the stainless steel rod and glass particles in this experiment.

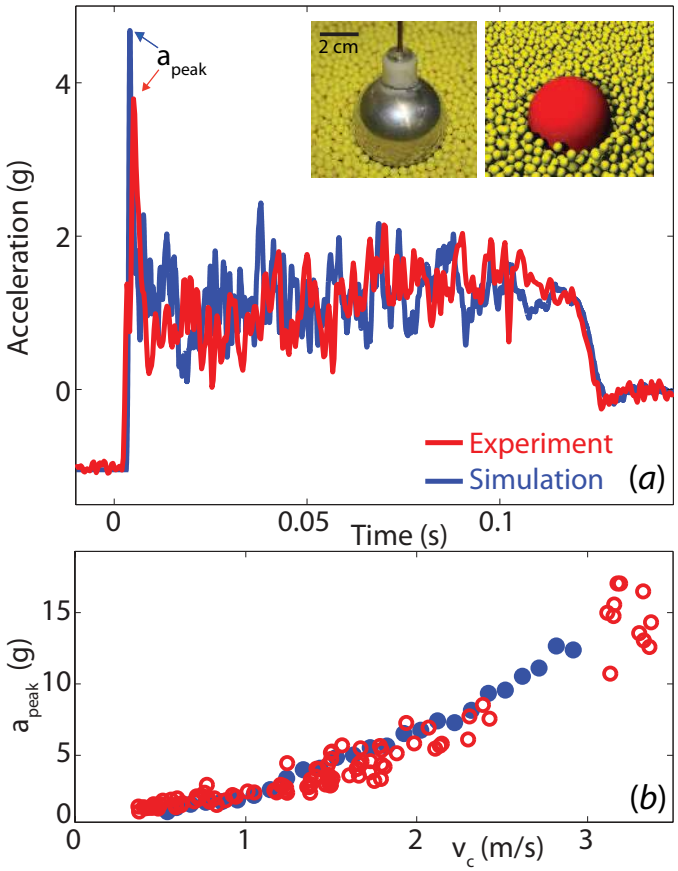

Figure S2: Validating the numerical simulation for 6 mm plastic spheres using the measured acceleration of a sphere during impact after free-fall (*2*). (a) Acceleration vs. time in simulation (blue) and experiment (red) with impact velocity of 1.4 m/s for a representative run. Acceleration is given in units of g, the acceleration due to gravity. (Left inset) Aluminum ball instrumented with accelerometer resting on 6 mm plastic spheres. (Right inset) Ball and particles in simulation. (b) Peak acceleration during impact as a function of impact velocity from simulation (blue) and experiment (red). Parameters for this numerical simulation are given in table S1.

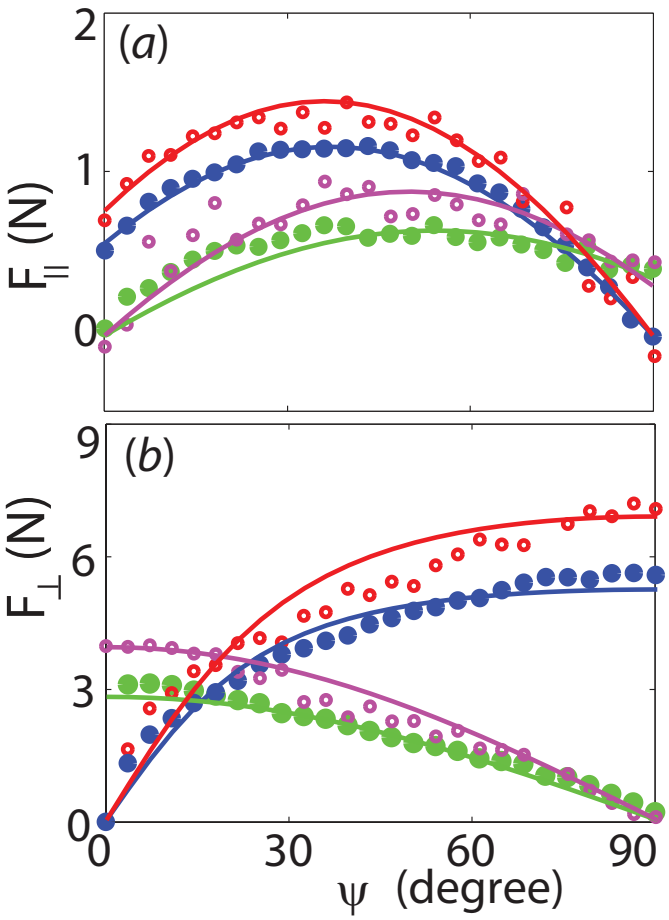

Figure S3: Forces ((a) $F_{\parallel}$ and (b) $F_{\perp}$) on a square cross-section rod (width, height $= 16$ mm, length $= 40$ mm) dragged through **3 mm glass** particles in simulation as a function of the angle, ψ, between the velocity direction and the rod axis. Blue and red markers correspond to forces along the length of the rod while green and magenta markers correspond to forces at the end caps of the rod. Filled and open circles correspond to loosely and closely packed media, respectively. Parameters for the simulation are given in table S1. Solid lines denote fits to equation (20) with fit parameters given in table S3.

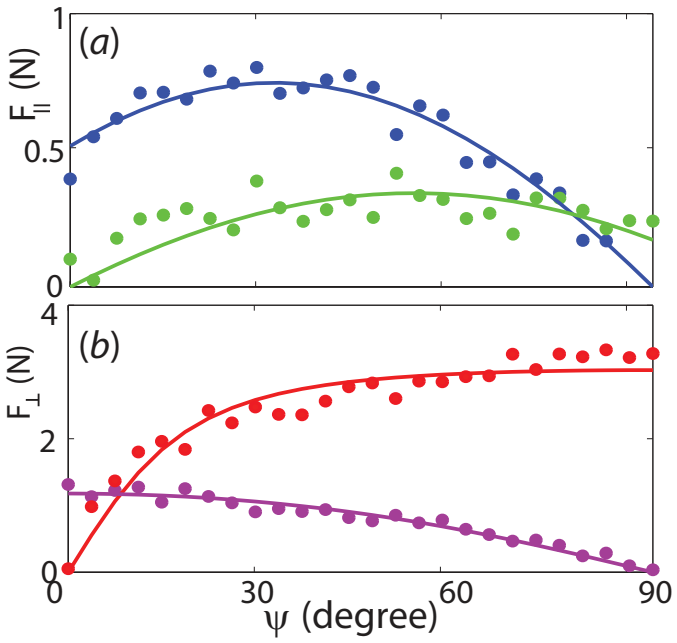

Figure S4: Forces ((a) $F_{\parallel}$ and (b) $F_{\perp}$) on a square cross-section rod (width, height $=$ 16 mm, length $=$ 70 mm) dragged through loosely packed **6 mm plastic** particles in simulation as a function of the angle, ψ, between the velocity direction and the rod axis. Blue and red markers correspond to forces along the length of the rod while green and magenta markers correspond to forces at the end caps of the rod. Parameters for the simulation are given in table S1. Solid lines denote fits to equation (20) with fit parameters given in table S3.

Description of supplementary movies

Movie S1 (722 KB): High speed x-ray video (250 fps) of the sandfish swimming within 3 mm glass particles. For details see §2 of main text.

Movie S2 (666 KB): Top view of a numerically simulated sandfish that swims like the animal in a validated numerical simulation of 3 mm glass particles. Particles above the sandfish model are rendered transparent. The sandfish model oscillates at 2.5 Hz. For details see §4.1 of main text.

Movie S3 (2.3 MB): Top view of a 7-segment sandfish robot swimming within 6 mm plastic particles. The markers on the mast of the robot indicate the location of head and tail segments. The robot is oscillating at 0.25 Hz. The video data is collected at 100 fps. For details see §4.2 of main text.

Movie S4 (2.5 MB): Top view of a numerically simulated 7 segment robot that swims like the physical robot in a validated numerical simulation of 6 mm plastic particles. Particles above the sandfish model are rendered transparent. For details see §4.2 of main text.

Table S1: Parameters used in simulation and measured from experiments.

6 mm plastic particles:

	Experiment	Simulation
Hardness (k)	1.7×10^8 kg s^{-2} m$^{-1/2}$	2×10^5 kg s^{-2} m$^{-1/2}$
Restitution coefficient	0.96	0.88
G_n	1×10^2 kg m$^{-1/2}$ s^{-1}	5 kg m$^{-1/2}$ s^{-1}
$\mu_{particle-particle}$ (μ_{pp})	0.073	0.080
$\mu_{body-particle}$ (μ_{bp})	0.27	0.27
Density	1.03 ± 0.04 g cm^{-3}	1.06 g cm^{-3}
Diameter	5.87 $\pm$ 0.06 mm	5.81 mm (50%) and 5.93 mm (50%)
Granular volume	188 PD $\times$ 62 PD $\times$ 35 PD	188 PD $\times$ 62 PD $\times$ 24 PD

PD is the average particle diameter of 5.87 mm. For both 6 mm plastic and 3 mm glass particles (see below) the restitution coefficient was measured for particle-particle collisions with one particle glued to a stainless steel plate and with an impact velocity of 0.48 m/s in experiment and simulation.

3 mm glass particles:

	Experiment	Simulation
Hardness (k)	5.7×10^9 kg s^{-2} m$^{-1/2}$	2×10^6 kg s^{-2} m$^{-1/2}$
Restitution coefficient	0.92 ± 0.03	0.88
G_n	15×10^2 kg m$^{-1/2}$ s^{-1}	15 kg m$^{-1/2}$ s^{-1}
$\mu_{particle-particle}$	0.10	0.10
$\mu_{particle-body}$	0.27	0.27
Density	2.47 g cm^{-3}	2.47 g cm^{-3}
Diameter	3.2 $\pm$ 0.2 mm	3.0 mm (50%) and 3.4 mm (50%)
Granular volume	67 PD $\times$ 56 PD $\times$ 31 PD	109 PD $\times$ 43 PD $\times$ 32 PD

PD is the average particle diameter of 3.2 mm.

Sandfish:

	Experiment	Simulation
Amplitude/Wavelength	0.25 ± 0.05	$0.06 - 0.53$
Length (snout to tail tip)	12.8 ± 0.3 cm	12 cm
Weight	16.2 ± 4 g	16 g
Maximum width	1.63 ± 0.11 cm	1.6 cm

Where error is unspecified for experiment, the value is accurate to the last significant digit.

Table S2: Fitting parameters for the linear approximations for the force laws in the analytical approximate solutions to the RFT.

	Region 1	Region 2	Region 3
$C_{\perp}^{n}$	0	0.36	1.3
$C_{S\perp}^{n}$	0.79	0.3	0
$C_{\parallel}^{n}$	0.27	0	0.14
$C_{S\parallel}^{n}$	0	0.16	0.074

Units for all values are N/cm^2 and 'n' denotes the region index.

Table S3: Fitting parameters for the analytical functions approximating $F_{\perp}$ and $F_{\parallel}$.

	C_S	C_F	C_L	γ
3mm particles LP length	5.57	2.30	-1.74	1.93
3mm particles LP end cap	19.52	1.24	-0.99	0.14
3mm particles CP length	7.70	2.79	-2.03	1.575
3mm particles CP end cap	42.16	1.87	-1.58	0.088
6mm particles length	3.21	1.34	-0.82	2.79
6mm particles end cap	0.73	0.30	-0.19	0.52

Units for C_S, C_F and C_L are N and unit for γ is dimensionless.